Ore Geology Reviews 153 (2023) 105261

Contents lists available at ScienceDirect

Ore Geology Reviews

journal homepage: www.elsevier.com/locate/oregeorev

Mineralogical distribution and genetic aspects of cobalt at the active Fåvne and Loki's Castle seafloor massive sulfide deposits, Arctic Mid-Ocean Ridges

Fredrik Sahlström [a,b,*], Sabina Strmić Palinkaš [b,c], Siv Hjorth Dundas [c], Eszter Sendula [b], Yanbo Cheng [d], Marie Wold [c], Rolf B. Pedersen [c]

[a] Geological Engineering Program, Pontificia Universidad Católica del Perú, San Miguel 15088, Lima, Peru
[b] Department of Geosciences, UiT The Arctic University of Norway, N-9037 Tromsø, Norway
[c] Centre for Deep Sea Research, Department of Earth Science, University of Bergen, N-5007 Bergen, Norway
[d] Geoscience Australia, GPO Box 378, Canberra, ACT 2601, Australia

ARTICLE INFO

Keywords:
Seafloor massive sulfide deposit
Fåvne
Loki's Castle
Ore mineralogy
Cobalt
LA-ICP-MS

ABSTRACT

The demand for responsibly sourced cobalt has increased dramatically as a result of the global transition to 'fossil-free' electromobility. However, the distribution, mineralogical expressions and mechanisms of concentration of Co in different types of hydrothermal ore deposits remain poorly constrained, inhibiting resource assessments and exploration. Here we report Co and other metal concentrations in ores from the active Fåvne and Loki's Castle seafloor massive sulfide (SMS) deposits located along the Mohns Ridge and assess some genetic aspects of Co. The assemblages from the recently discovered Fåvne deposit are dominated by either pyrrhotite-isocubanite or sphalerite, in both cases with abundant anhydrite and local Fe-oxides. They show high whole-rock Co concentrations (average 0.31 wt%, up to 0.98 wt%) and Co is enriched in the Cu-rich relative to the Zn-rich assemblages. No independent Co-minerals are observed; rather, Co is variably hosted in pyrrhotite (up to 1.03 wt %), isocubanite (up to 0.71 wt%), sphalerite (up to 0.14 wt%) and magnetite (~100 ppm). The assemblages from Loki's Castle are dominated by pyrrhotite, isocubanite, sphalerite, amorphous silica and barite, and they exhibit distinctly lower Co concentrations in both whole-rock samples (average 62 ppm, up to 368 ppm) and in individual minerals (up to 152, 148 and 99 ppm in isocubanite, sphalerite and pyrrhotite, respectively). At both deposits, Co is interpreted to enter the Fe-, Cu-Fe- and Zn-sulfides and Fe-oxides via simple $Co^{2+} \leftrightarrow (Fe,Zn)^{2+}$ substitutions and its mineralogical distribution reflects a combination of crystal-chemical controls (e.g., spin state compatibility between Co^{2+} and the divalent cation) and changing hydrothermal fluid conditions (e.g., temperature) during mineral formation. Based on a comparison with global SMS and VMS deposits, we suggest that the 'diffuse' high-temperature venting at Fåvne can in part explain the enrichment of Co in the surficial sulfides, whereas at Loki's Castle more Co-rich sulfides might occur in the interior of the deposit. Furthermore, Fåvne and several Co-rich deposits elsewhere show evidence for the involvement of saline hydrothermal fluids with enhanced capacity to mobilize and transport Co during their evolution. While their future role as a source of Co and other critical commodities remains uncertain, active SMS deposits provide unique insights into the processes and conditions associated with formation of hydrothermal Co mineralization that will aid both deep-sea and onshore exploration.

1. Introduction

The physical, magnetic and electrical properties of cobalt (Co) make it a critical component in a range of modern industrial and technological applications, not least in cathodes in rechargeable Li-ion batteries (Slack et al., 2017; Shedd et al., 2017; Hitzman et al., 2017). The demand for Co has therefore increased dramatically as a result of the ongoing global transition to 'fossil-free' electromobility (Alves Dias et al., 2018). This demand, coupled with the poor sustainability and supply-security in the main Co-producing regions (DR Congo, >70 % of global Co mine

* Corresponding author at: Geological Engineering Program, Pontificia Universidad Católica del Perú, San Miguel 15088, Lima, Peru.
E-mail address: fsahlstrom@pucp.edu.pe (F. Sahlström).

https://doi.org/10.1016/j.oregeorev.2022.105261
Received 6 June 2022; Received in revised form 28 November 2022; Accepted 13 December 2022
Available online 16 December 2022
0169-1368/© 2022 The Author(s). Published by Elsevier B.V. This is an open access article under the CC BY license (http://creativecommons.org/licenses/by/4.0/).

production in 2021, and China, the current leading producer of refined Co; Banza Lubaba Nkulu et al., 2009; Banza Lubaba Nkulu et al., 2018; Shedd et al., 2017; Sovacool, 2019; Gulley et al., 2019; U.S. Geological Survey, 2022), have sparked a global effort to identify and characterize new potential Co resources in a variety of geologic environments (Slack et al., 2017; Petavratzi et al., 2019; Horn et al., 2021).

Apart from the approximately 70 currently known discrete Co minerals, Co can also be incorporated in economically significant concentrations ($\gtrsim$ 0.1 wt% Co; Smith, 2001) in the crystal lattices of several common sulfides, silicates, oxides and oxyhydroxides, with sulfides accounting for the majority of Co production (Donaldson and Beyersmann, 2010; Mudd et al., 2013). Current recovery of Co from terrestrial resources (~25 Mt) is primarily as a byproduct of Cu or Ni mining, and the dominant sources are sedimentary rock-hosted, stratabound Cu deposits, magmatic sulfide Ni-Cu deposits, and laterite Ni deposits (Smith, 2001; Mudd et al., 2013; Slack et al., 2017, U.S. Geological Survey, 2022). A significantly larger Co resource (>120 Mt) has been identified on the global seafloor, the majority of which occurs in manganese nodules and ferromanganese crusts (Manheim, 1986; Hein et al., 2013; Petersen et al., 2016; U.S. Geological Survey 2022). Moreover, recent exploration and research has indicated that some seafloor massive sulfide (SMS) deposits forming along volcanically active plate boundaries also contain significant Co concentrations (Fouquet et al., 2010). In addition to being a potential future source of Co (e.g., Slack et al., 2017), active SMS deposits provide a natural laboratory to study processes and conditions associated with formation of hydrothermal Co mineralization.

The Arctic Mid-Ocean Ridges (AMOR) are a ~ 4,000 km long, ultraslow-spreading ridge system that extends from the northern shelf of Iceland to the Siberian Shelf in the Laptev Sea (Pedersen et al., 2010b). The AMOR system comprises six major ridge segments that from south to north include the Kolbeinsey Ridge, the Mohns Ridge, the Knipovich Ridge, the Molloy Ridge, the Lena Trough, and the Gakkel Ridge (Fig. 1a; Pedersen et al., 2010b; Pedersen and Bjerkgård, 2016). The southern part of the AMOR is characterized by increased magmatic activity, anomalously thick crust and elevated topography due to the influence of the Iceland and Jan Mayen hot spots (Kodaira et al., 1998; Pedersen et al., 2010b; Elkins et al., 2016). Toward the north, magmatic activity and crustal thickness gradually decrease, spreading centers and rift valleys become deeper and more pronounced, and low-angle detachment faults with up to ~ 10 km displacements are locally developed (Géli et al., 1994; Michael et al., 2003; Pedersen and Bjerkgård, 2016). The first discovery of an active high-temperature black smoker vent field with associated SMS mineralization along the AMOR was Loki's Castle on the northern Mohns Ridge in 2008 (Fig. 1; Pedersen et al., 2010a). Since then, continued exploration and research has resulted in several additional discoveries including the active Fåvne deposit on the central Mohns Ridge in 2018 (Fig. 1; Stenløkk et al., 2019). Among the geologically and geochemically diverse SMS deposits along the AMOR, Fåvne stands out for its high Co concentration (up to ~ 1 wt% Co in grab samples; Strmić Palinkaš et al., 2020; Norwegian Petroleum Directorate, 2022) and its discovery has highlighted the exploration potential for Co in the area.

In this contribution, we document ore mineral assemblages from the active Fåvne and Loki's Castle SMS deposits and determine their whole-rock and mineral chemical compositions. The new data are integrated with observations from comparable deposits globally with the primary aim of improving the understanding of the mineralogical distribution and genetic aspects of Co in SMS deposits. The results of our study may aid future exploration for Co in SMS deposits along the AMOR and similar tectonic settings globally, as well as in fossil analogs [i.e., volcanogenic massive sulfide (VMS) deposits] preserved in volcanic suites onshore.

2. Geologic setting

2.1. Fåvne

The Fåvne SMS deposit (72°45′N, 3°50′E) was discovered at ~ 3,000 m water depth in the central part of the Mohns Ridge during an expedition led by the Norwegian Petroleum Directorate in 2018 (Fig. 1; Stenløkk et al., 2019). It is located at the floor of the rift valley northwest of a large axial volcanic ridge (AVR), immediately adjacent to the foot of a ~ 500 m tall hill. The hill represents the fault scarp of the footwall of the main bounding normal fault to the rift valley and this structure is suggested to localize heat and hydrothermal fluid flow (Brekke et al., 2021). Hydrothermal activity at Fåvne occurs within a ~ 40,000 m^2, flat-lying field principally composed of basalt lava and breccia covered by a ~ 50 cm thick layer of deep-marine sediments. Thus far, no ultramafic rocks have been recovered during seafloor sampling (Brekke et al., 2021). However, the tectonic setting of Fåvne is similar to those of ultramafic-hosted SMS and VMS deposits elsewhere (i.e., along a major low-angle normal fault; Fouquet et al., 2010; Patten et al., 2022), and due to anomalously thin oceanic crust in the area (Klingelhöfer et al., 2000) ultramafic rock complexes are expected to be within the reach of the hydrothermal system.

The relatively small sulfide deposit has an overall flat morphology and is made up of nine individual mound structures with associated chimney complexes (Pedersen et al., 2021). The largest mound measures 40 × 15 m (basal diameter × height) and is located in the southern part of the hydrothermal field that is currently characterized by low-temperature venting and Fe-oxyhydroxide-rich precipitation. In turn, five of the mounds in the central and northern parts of the field discharge high-temperature (up to ~ 280 °C) black smokers and range in size from 15 × 6 to 30 × 10 m (Pedersen et al., 2021). The inactive Gnitahei deposit is located at the fault scarp ~ 700 m southwest of Fåvne (Fig. 1). It comprises pyrite-dominated, sub-seafloor replacement-type mineralization in altered basalt and is suggested to represent an earlier stage of hydrothermal activity along the same active normal fault that currently focusses hydrothermal fluid flow beneath Fåvne.

2.2. Loki's Castle

The Loki's Castle SMS deposit (73°34′N, 8°9′E) is situated near the summit of a ~ 30 km long and ~ 800 m high AVR, where the Mohns Ridge passes into the Knipovich Ridge via an almost perpendicular northward bend of the ridge axis (Fig. 1; Pedersen et al., 2010a; Baumberger et al., 2016a). Dome-shaped core complexes that locally expose lower crustal and upper mantle rocks occur on the western flank of the AVR, whereas the eastern flank is covered by sediments belonging to the distal parts of the Bear Island Fan. These sediments have spilled into the rift valley surrounding the AVR and have infilled half-graben basins on the western flank (Fig. 1b; Bruvoll et al., 2009; Pedersen et al., 2010a; Pedersen et al., 2010b; Baumberger et al., 2016b).

Venting occurs at ~ 2,400 m water depth and is controlled by two northeast-striking normal faults that define the northwest margin of a ~ 50–100 m deep rift that extends along the crest of the AVR (Pedersen et al., 2010a). Hot (300–320 °C) black smokers are emitted from four distinct chimney structures that are each up to ~ 13 m tall and located on top of two separate but coalescing sulfide mounds. The western mound (containing the *Menorah*, *Camel* and *Sleepy* chimneys) and the eastern mound (*João* chimney) have their centers ~ 150 m apart and are each ~ 20–30 m high and ~ 150–200 m wide at the base (Baumberger et al., 2016b), forming a composite mound with a size comparable to that of the Trans-Atlantic Geotraverse (TAG) mound on the Mid-Atlantic Ridge (Humphris et al., 1995). Additionally, a low-temperature (~20 °C) vent area featuring numerous small barite-silica chimneys occurs adjacent to the eastern mound (Eickmann et al., 2014). While Loki's Castle has developed on bare mafic substrate, the chemical and isotopic signatures of the vent fluids record a strong influence of the Bear

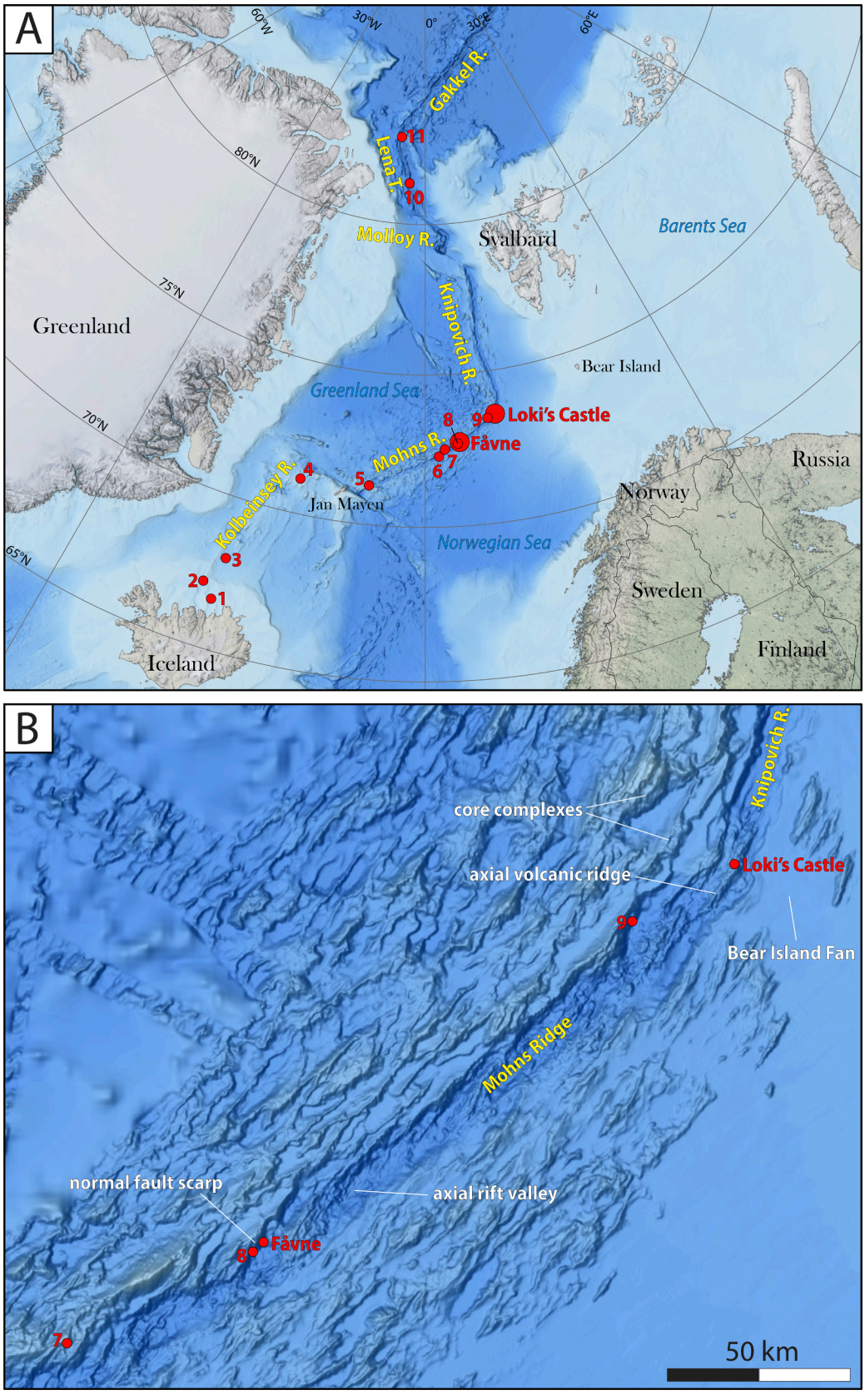

Fig. 1. (**A**) Bathymetric map showing the locations of the Fåvne and Loki's Castle SMS deposits and other known sulfide occurrences (red symbols) along the Arctic Mid-Ocean Ridges: 1) Grimsey; 2) Kolbeinsey; 3) Squid Forest; 4) Seven Sisters; 5) Soria Moria/Troll Wall/Perle and Bruse; 6) Ægirs Kilde; 7) Copper Hill; 8) Gnitahei; 9) Mohns Treasure; 10) Lucky B; 11) Aurora. Modified from Pedersen and Bjerkgård (2016) using basemap from NOAA (2020). (**B**) Close-up of the northern part of the Mohns Ridge. (For interpretation of the references to colour in this figure legend, the reader is referred to the web version of this article.)

Island sediments that most likely also occur buried within the stratigraphic footwall sequence (Baumberger et al., 2016a; Baumberger et al., 2016b).

3. Materials and methods

3.1. Sampling

Mineralized samples from Fåvne and Loki's Castle were originally collected using an *Ægir* 6000 remotely operated underwater vehicle (ROV) deployed from R/V *G.O. Sars* during cruises led by the Centre for Deep Sea Research (University of Bergen) in the summers of 2017, 2019 and 2020. Samples from Fåvne available for this study included sulfide chimney fragments from several of the mounds associated with high-temperature venting in the central and northern parts of the field (n = 9). From Loki's Castle, sulfide chimney fragments from the western mound (n = 7) and a sulfide crust from the eastern mound (n = 1) were included.

All samples were cut and prepared as polished thick sections and subsequently characterized by means of reflected polarized light microscopy. A subset of the samples was selected for additional electron microscopy studies and whole-rock and mineral chemical analyses, as outlined below. The primary goal of these analyses was to determine the Co concentrations in the Fåvne and Loki's Castle assemblages. For comparisons throughout this paper, we use the terms 'high' and 'Co-rich' to refer to Co concentrations $\gtrsim$ 0.1 wt%, based on typical economic grades in land-based ores (Smith, 2001).

3.2. Electron microscopy and mineral major element analysis

Mineralogical characterization by means of backscattered electron (BSE) imaging coupled with energy-dispersive X-ray spectroscopy (EDS) was done using a Zeiss Merlin Compact VP field emission scanning electron microscope (FE-SEM) with an Oxford Instruments X-Max EDS system at the Department of Geosciences, UiT The Arctic University of Norway. Major elements in sulfides were analyzed on the same instrument using an attached Oxford Instruments INCA Wave wavelength-dispersive X-ray spectroscopy (WDS) system. The WDS analyses were done with a focused (<1 μm diameter) beam with an acceleration voltage of 15 kV and a current of 10 nA. Analytical conditions were [analyzed element (standard, emission, crystal)]: Cu (chalcopyrite, Kα, LIF), Fe (pyrite, Kα, LIF), Zn (sphalerite, Kα, LIF) and S (pyrite, Kα, PET).

3.3. Whole-rock geochemical analysis

Whole-rock geochemical analyses were done at the laboratories of ALS, Vancouver, Canada. Representative sample splits were pulverized and subsequently analyzed using a combination of methods, which include (ALS, 2021): lithium borate fusion with ICP-AES finish (ME-ICP06; for SiO_2, Fe_2O_3, CaO, MnO and BaO), induction furnace with IR finish (ME-IR08; for S), lithium borate fusion with ICP-MS finish (ME-MS81; for Ba, Cr, Ga, Ge, Sn and V), aqua regia digestion with ICP-MS finish (ME-MS42; for As, Bi, Hg, In, Sb, Se, Te and Tl), four-acid digestion with ICP-AES finish (ME-4ACD81; for Ag, Cd, Co, Cu, Mo, Ni, Pb and Zn), and fire assay fusion with AAS finish (Au-AA23; for Au). For samples that had higher concentrations of specific elements than the upper detection limits of these methods, Cu, Zn and/or Pb were re-analyzed using four-acid digestion with ICP-AES finish (OG62) whereas As, Se and/or Hg were re-analyzed using aqua regia digestion with ICP-AES finish (ME-ICP41).

3.4. Mineral trace element analysis and mapping

In-situ trace element analyses of pyrrhotite, pyrite, isocubanite and sphalerite were done by laser ablation inductively coupled plasma mass spectrometry (LA-ICP-MS) using a Nu Instruments AttomES High Resolution ICP-MS coupled to a Resonetics RESOlution M−50−LR 193 nm excimer laser with a Laurin two-volume ablation cell, housed at the Department of Earth Science, University of Bergen. Laser parameters during spot analyses included a beam diameter of 19 or 26 μm, an energy of 40 mJ (attenuated 50 %) and a frequency of 5 Hz. Helium was used as carrier gas and was mixed with Ar prior to entering the ICP-MS. The collected analytes were: ^{34}S, ^{51}V, ^{53}Cr, ^{55}Mn, ^{57}Fe, ^{59}Co, ^{60}Ni, ^{63}Cu, ^{66}Zn, ^{71}Ga, ^{72}Ge, ^{75}As, ^{77}Se, ^{95}Mo, ^{107}Ag, ^{112}Cd, ^{115}In, ^{118}Sn, ^{121}Sb, ^{128}Te, ^{197}Au, ^{202}Hg, ^{205}Tl, ^{208}Pb and ^{209}Bi. A set of matrix-matched reference materials, including USGS MASS-1 (Wilson et al., 2002), STDGL3 (Danyushevsky et al., 2011; Belousov et al., 2015) and Aljustrel-2 (Garbe-Schönberg and Müller, 2014), were included in the analytical sequence and used jointly as bracketing external standards for data reduction (MASS-1 for S, V, Cr, Fe, Cu, Ga, Ge and Hg; STDGL3 for Mn, Co, Ni, Zn, As, Se, Mo, Ag, Cd, In, Sb, Te, Au, Tl, Pb and Bi; Aljustrel-2 for Sn) and as secondary standards to evaluate analytical accuracy. The isotopes used as internal standards for data quantification were ^{57}Fe (pyrrhotite and pyrite) and ^{63}Cu (isocubanite), based on concentrations measured previously by WDS (Electronic Supplementary Material 2). For sphalerite, internal standardization was done by normalizing the major cations (Zn and Fe) to 67 wt%. Additionally, a small number of magnetite grains were analyzed using the above sulfide protocol and a stoichiometric Fe value (72.36 wt%) for internal standardization. The magnetite data are therefore only considered semi-quantitative. Processing of spot data was done offline using the Iolite v. 4 software (Paton et al., 2011). During processing, signals or segments of signals showing evidence for major mineral inclusions beneath the sample surface were systematically excluded. However, a few elements (e.g., Bi) were below or close to the limit of detection in some minerals and exhibited erratic signals that were not mirrored by the more abundant suite of elements. Local enrichments in these elements may thus partly or wholly reflect microscopic inclusions and such data is reported.

We also performed trace element mapping of sulfide assemblages at the Geochemistry Laboratories of Trinity College Dublin. Mapping was done using a Teledyne Photon Machines Analyte G2 193 nm Ar-F excimer laser with a HelEx II two-volume ablation cell. The laser ablation system was coupled to a Thermo Scientific iCAP-Qc quadrupole ICP-MS utilizing a Teledyne Photon Machines Aerosol Rapid Introduction System. Helium was used as carrier gas in the ablation cell and Ar and N_2 were added at the ICP-MS interface to enhance signal sensitivity. Sets of parallel and overlapping line rasters were ablated sequentially across rectangular map areas and the laser beam size, fluence, repetition frequency, scan speed and dwell time were set according to the target sulfide grain sizes in each map (Zhou et al., 2020). The external standards MASS-1 and UQAC were measured at the beginning and at the end of each run to correct for mass bias and instrument drift. The measured isotopes were: ^{34}S, ^{57}Fe, ^{59}Co, ^{65}Cu, ^{66}Zn, ^{75}As, ^{92}Mo, ^{109}Ag, ^{115}In, ^{117}Sn, ^{121}Sb, ^{197}Au, ^{207}Pb and ^{209}Bi. Data reduction and production of qualitative (relative counts) element distribution images was done using the Iolite v. 3 software (Paton et al., 2011).

3.5. Fluid inclusion microthermometry

To address the lack of published information on the Fåvne hydrothermal fluids and to facilitate interpretations of our mineralogical and geochemical data, we performed auxiliary microthermometric measurements of fluid inclusions hosted in anhydrite within the studied assemblages. Petrographic descriptions of the fluid inclusions and full experimental details and results are provided in Electronic Supplementary Material 1.

4. Results

4.1. Ore petrography

4.1.1. Fåvne

The studied assemblages from Fåvne comprise anhydrite and semi-massive sulfides in the form of open-space fillings and crusts (Table 1; Fig. 2). They can be subdivided into Cu-rich and Zn-rich assemblages based on variations in sulfide mineralogy. The spatial distribution of the two assemblages at the scale of the hydrothermal field has not yet been documented in detail. At some chimney structures, Cu-rich assemblages occur at the base and Zn-rich assemblages at the top of the chimney (sample GS21- ROV07; Table 4).

The Cu-rich assemblages are dominated by anhedral to subhedral pyrrhotite crystals with equant to bladed shapes that occur intergrown with anhedral isocubanite crystals in aggregates (Fig. 2c, e). Chalcopyrite occurs as fine (~1 μm wide) lamellae within some isocubanite crystals (cf., Pruseth et al., 1999). Additionally, presumed secondary chalcopyrite with rare chalcocite and covellite occur locally along fractures and grain boundaries in isocubanite and along contacts between isocubanite and pyrrhotite. Minor sphalerite is locally present as anhedral to subhedral crystals and masses that both pre-date (Fig. 2c) and post-date the pyrrhotite-isocubanite aggregates. Rare pyrite is observed locally as fine (<50 μm diameter) individual crystals that have overgrown pyrrhotite and isocubanite.

The Zn-rich assemblages are dominated by sphalerite and no Cu-bearing minerals have been observed (Fig. 2d). Sphalerite occurs as anhedral to subhedral crystals (<500 μm diameter) and masses that locally exhibit well-developed growth banding. Variable amounts of pyrrhotite, pyrite and marcasite occur locally as fine, anhedral to subhedral crystals and aggregates within massive sphalerite or anhydrite.

Anhydrite precipitated throughout the paragenetic sequence in both the Cu-rich and the Zn-rich assemblages (Fig. 2b-e). Additionally, several types of Fe-oxides and Fe-oxyhydroxides are observed in both assemblages. Rare primary magnetite occurs locally as fine (<50 μm diameter), anhedral crystals that have been overgrown by pyrrhotite-isocubanite or sphalerite. Another primary Fe-oxide mineral, poorly crystalline and exhibiting skeletal and colloform textures, occurs as locally voluminous void fills that overprint the sulfide assemblages (Fig. 2e). Moreover, secondary goethite and ferrihydrite are locally abundant as oxidation products after pyrrhotite.

Table 1
List of identified minerals and their abundances in the studied assemblages from Fåvne and Loki's Castle. Major ≳15 %; Minor ~ 2–15 %; Rare ≲2%.

Mineral	Formula	Abundance
FÅVNE		
Anhydrite	$CaSO_4$	Major
Chalcocite	Cu_2S	Rare
Chalcopyrite	$CuFeS_2$	Minor
Covellite	CuS	Rare
Ferrihydrite	Fe_2O_3*$0.5H_2O$	Minor
Goethite	FeO(OH)	Minor
Iron oxide, amorphous	Fe, O (?)	Minor
Isocubanite	$CuFe_2S_3$	Major
Magnetite	Fe_3O_4	Rare
Pyrite	FeS_2	Minor
Pyrrhotite	$Fe_{1-x}S$	Major
Sphalerite	(Zn,Fe)S	Major
LOKI'S CASTLE		
Anglesite	$PbSO_4$	Rare
Anhydrite	$CaSO_4$	Minor
Arsenic, native	As	Rare
Barite	$BaSO_4$	Major
Chalcocite	Cu_2S	Rare
Chalcopyrite	$CuFeS_2$	Minor
Covellite	CuS	Rare
Ferrihydrite	Fe_2O_3*$0.5H_2O$	Minor
Goethite	FeO(OH)	Minor
Galena	PbS	Minor
Isocubanite	$CuFe_2S_3$	Major
Lepidocrocite	FeO(OH)	Rare
Marcasite	FeS_2	Minor
Mn(-Pb-Cu)-oxide, amorphous	Pb, Cu, Mn, O (?)	Rare
Pyrite	FeS_2	Minor
Pyrrhotite	$Fe_{1-x}S$	Major
Silica, amorphous	SiO_2	Major
Sphalerite	(Zn,Fe)S	Major
Talc	$Mg_3Si_4O_{10}(OH)_2$	Minor

4.1.2. Loki's Castle

The studied chimney fragments from the western mound at Loki's Castle are typically zoned, with cores of pyrrhotite-dominated, semi-massive to massive sulfides that are surrounded by a ~ 1 cm thick layer of light-colored, barite-silica-rich material (Table 1; Fig. 3a). The grain size of the sulfides generally decreases toward the barite-silica caps, and a fluid-induced 'breaching' texture of the barite-silica caps by sulfides is locally visible (Fig. 3a). The single studied sample from the eastern mound comprises semi-massive sulfide crusts that grew outward from talc-anhydrite-dominated substrate (Fig. 3b).

The sulfide mineralogy and paragenetic sequence are similar in all studied samples (see also da Cruz, 2015; Snook et al., 2018). Early-formed sphalerite and isocubanite occur in variably sized aggregates of anhedral crystals that locally exhibit skeletal and dendritic textures (Fig. 3a-d). Textural relations indicate that sphalerite has been partly replaced by isocubanite (Fig. 3b). Similar to at Fåvne, primary chalcopyrite occurs as fine lamellae within some isocubanite crystals, whereas presumed secondary chalcopyrite with rare chalcocite and covellite occur as delicate coatings along fractures and grain boundaries in isocubanite. The sphalerite-isocubanite aggregates are overprinted by voluminous networks of anhedral to subhedral, platy pyrrhotite crystals of variable size, producing a porous rock (Fig. 3a-d). Pyrrhotite is variably oxidized and replaced by secondary goethite, ferrihydrite and lepidocrocite (Fig. 3d). Galena is commonly present as fine (<5 μm diameter) anhedral crystals that occur either intergrown with sphalerite and isocubanite or as inclusions in pyrrhotite (Fig. 3c). Large amounts (~50 modal %) of pyrite and marcasite are only observed in one single sample where they form delicate aggregates that overprint and encrust earlier-formed sphalerite, isocubanite and pyrrhotite (Fig. 3d). The identified gangue minerals in the Loki's Castle assemblages include amorphous silica, barite, talc, anhydrite, and rare anglesite; amorphous silica and barite are also the main components of the barite-silica caps (Fig. 3a-b, e-f). The barite-silica caps contain small amounts of very fine-grained sulfides, primarily in the amorphous silica domains. Here, pyrite and marcasite exhibit colloform textures and are locally overgrown by native arsenic (Fig. 3f). The barite-silica caps also contain late-stage void fills of a poorly crystalline, Pb-Cu-bearing Mn-oxide mineral exhibiting colloform and botryoidal textures (Fig. 3e). The mineral shows similarities to Mn-oxides from the Seven Sisters vent field on the Kolbeinsey Ridge (Fig. 1a; Marques et al., 2020) and from some submarine hydrothermal Mn-Fe-Si precipitates (e.g., Utu Uli, Anakele and Utu Sega deposits, Wallis and Futuna; Pelleter et al., 2017).

4.2. Whole-rock geochemistry

4.2.1. Fåvne

The Cu-rich assemblages from Fåvne exhibit high whole-rock concentrations of Cu (up to 9.2 wt%) and Co (up to 0.98 wt%), whereas Zn (up to 1540 ppm) and Pb (up to 6 ppm) concentrations are low (n = 4; Table 2; Fig. 4). The Au and Ag concentrations reach 1.6 and 6 ppm, respectively, and Au:Ag ratios vary between 0.02 and 0.3. Other elements locally present in concentrations above 10 ppm include As (up to 38 ppm) and Mo (up to 12 ppm).

The Zn-rich assemblages have distinctly higher Zn (up to 31.15 wt%) but lower Cu (up to 3260 ppm) and Co (up to 1525 ppm) concentrations than the Cu-rich assemblages (n = 4; Table 2; Fig. 4). These assemblages

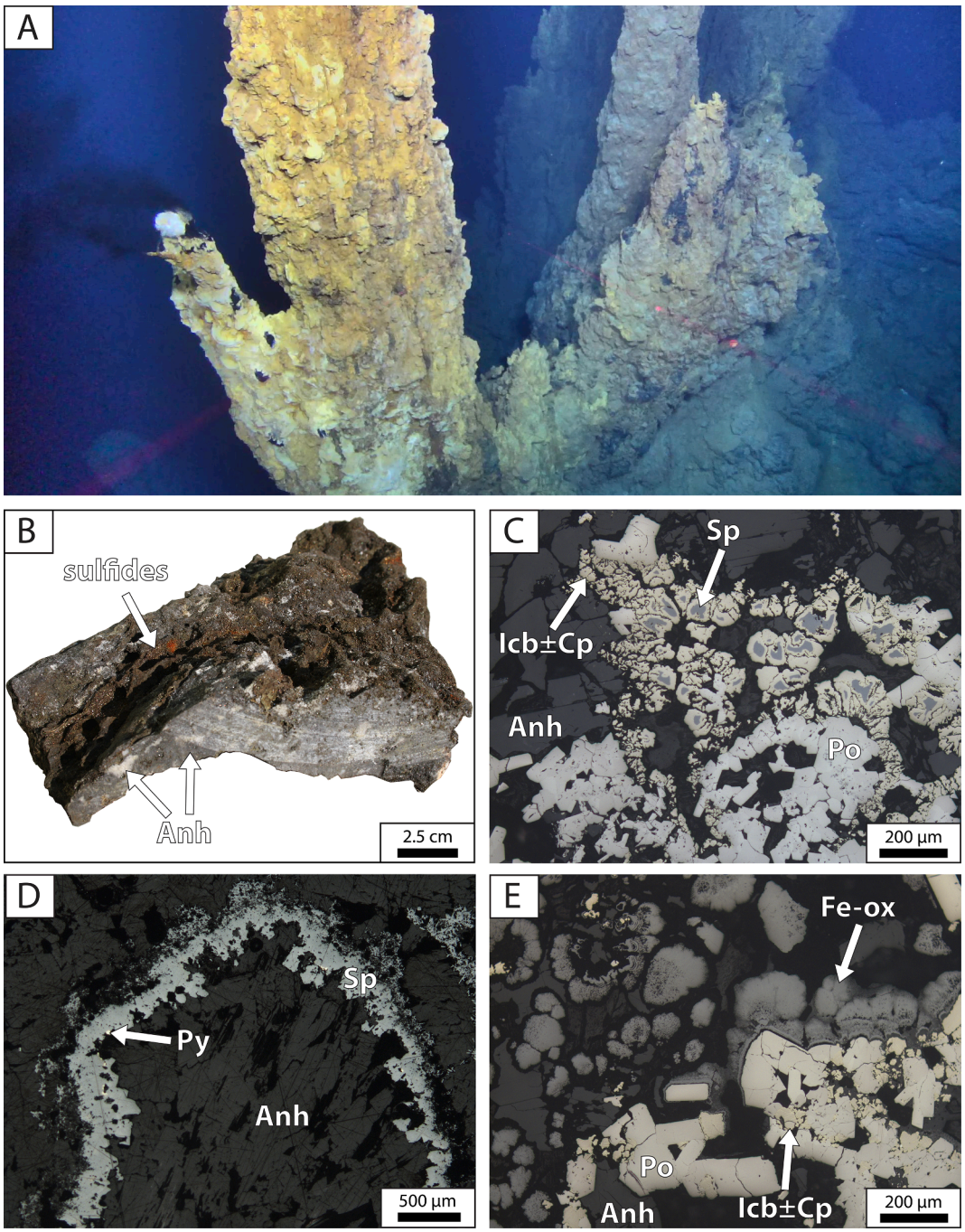

Fig. 2. Photographs and photomicrographs of ore assemblages from Fåvne. (**A**) Active sulfide chimney structure with black smokers discharging from a sphalerite-dominated edifice. (**B**) Chimney fragment comprising Cu-rich semi-massive sulfides and anhydrite. (**C**) Assemblage of intergrown pyrrhotite, isocubanite and anhydrite. Sphalerite occurs as partially replaced inclusions in isocubanite (reflected light, plane polarized). (**D**) Crust of massive sphalerite with minor pyrite lining a vug in anhydrite. Following sphalerite precipitation, the vug was infilled by anhydrite (reflected light, plane polarized). (**E**) Assemblage of pyrrhotite, isocubanite and anhydrite (partly removed during polishing) infilled by a poorly crystalline Fe-oxide mineral exhibiting colloform and skeletal textures. Both primary and presumed secondary chalcopyrite (yellow, poorly visible in photo) is present within isocubanite crystals (reflected light, plane polarized). Abbreviations: Anh – anhydrite; Cp – chalcopyrite; Fe-ox – Fe-oxide; Icb – isocubanite; Po – pyrrhotite; Py – pyrite; Sp – sphalerite. (For interpretation of the references to colour in this figure legend, the reader is referred to the web version of this article.)

also have lower Au (up to 0.05 ppm) but higher Ag (up to 99 ppm) concentrations, resulting in very low Au/Ag ratios (0.0003–0.0008). Other elements locally present in concentrations above 100 ppm include Cd, Pb and Sn, and elements locally above 10 ppm include Mo, Sb, Ga and Ge. The Zn-rich assemblages also show subtle enrichment in Se, Hg and Tl, but depletion in As, In and Bi, relative to the Cu-rich assemblages (Table 2). The concentrations of Si (up to 0.15 wt%) and Ba (up to 39 ppm) are low in both the Cu-rich and Zn-rich assemblages.

Several mineralogical–geochemical features at Fåvne (e.g., the pyrrhotite-isocubanite-sphalerite-anhydrite-dominated and silica-poor assemblages, abundant primary Fe-oxides, high Co and Cu + Zn concentrations) are similar to those observed at ultramafic-hosted and suspected ultramafic-influenced SMS deposits globally (Mozgova et al., 1999, 2008; Bogdanov et al., 2002; Lein et al., 2003; Marques et al., 2006, Fouquet et al., 2010; Wang et al., 2014, 2018; Webber et al., 2015; Firstova et al., 2016; Liao et al., 2018; Toffolo et al., 2020; Choi et al.,

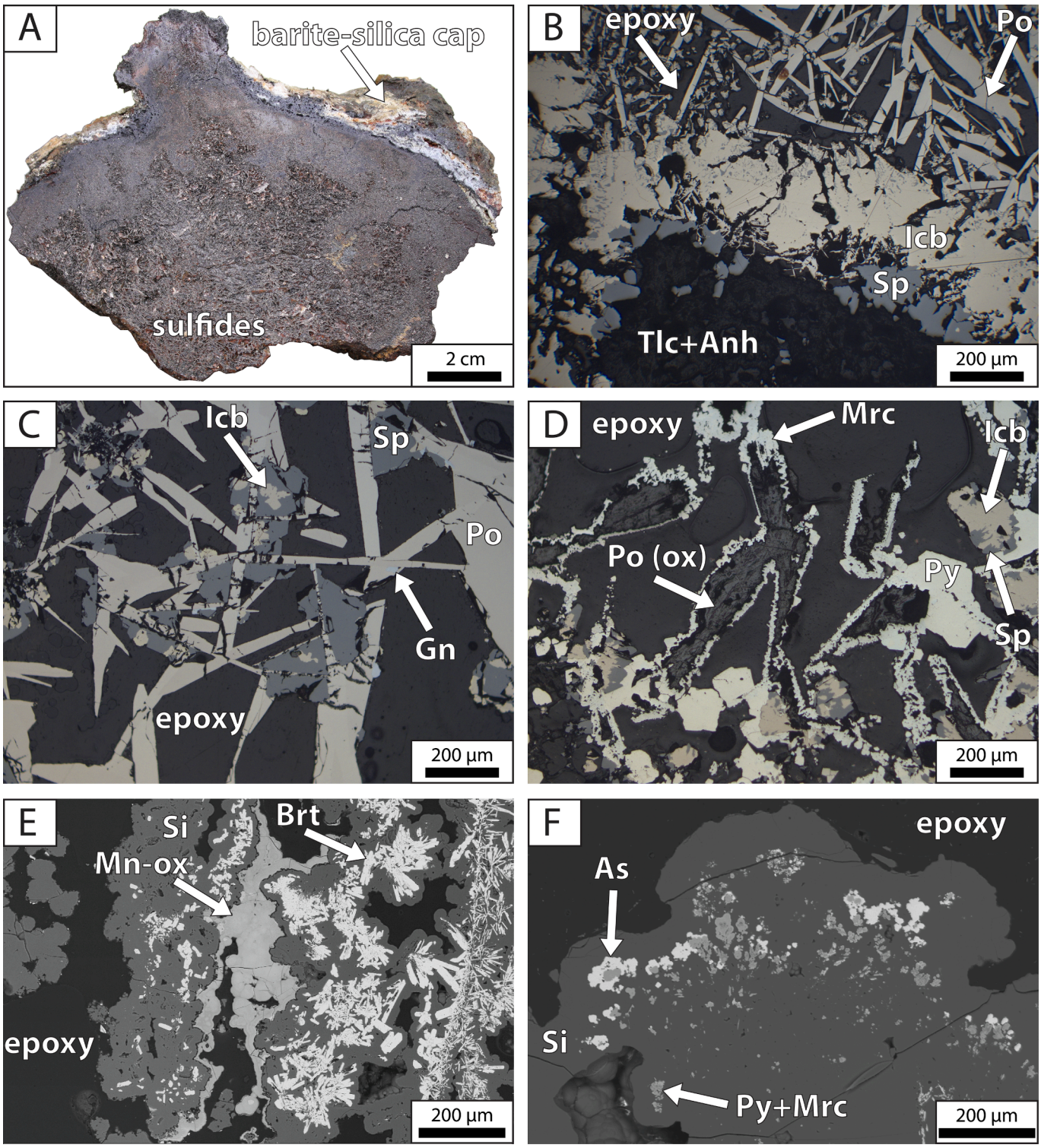

Fig. 3. Photographs, photomicrographs and backscattered electron (BSE) images of ore assemblages from Loki's Castle. (**A**) Chimney fragment featuring a massive sulfide core and a ~ 1 cm thick barite-silica cap. Note the fluid-induced 'breaching' texture in the upper part of the sample. (**B**) Crust of semi-massive to massive sulfides developed around a fragment of talc and anhydrite. The sulfide crystallization sequence is interpreted as: sphalerite → isocubanite → pyrrhotite (reflected light, plane polarized). (**C**) Sphalerite-isocubanite-galena assemblage overprinted by networks of platy pyrrhotite crystals (reflected light, plane polarized). (**D**) Delicate aggregates of pyrite and marcasite overprinting and encrusting earlier-formed sphalerite, isocubanite and (now oxidized) pyrrhotite (reflected light, plane polarized). (**E**) Assemblage from a barite-silica cap (cf., Fig. 3a) comprising amorphous silica, barite and a not fully characterized Mn-oxide mineral with colloform and botryoidal texture (BSE image). (**F**) Native arsenic overprinting fine-grained pyrite and marcasite within a barite-silica cap (BSE image). Abbreviations: Anh – anhydrite; As – native arsenic; Brt – barite; Gn – galena; Icb – isocubanite; Mn-ox – Mn-oxide; Mrc – marcasite; Po – pyrrhotite; Py – pyrite; Si – amorphous silica; Sp – sphalerite: Tlc – talc.

Table 2
Summary of whole-rock geochemical data for Fåvne and Loki's Castle. The data is reported in parts per million (1 ppm = 1 mg/kg) unless noted otherwise. Elements marked with '<' were below the indicated detection limits and elements marked with '–' were not analyzed.

Sample ID	Rock type	Si (%)	Ca (%)	S (%)	Ba	V	Cr	Mn	Fe (%)	Co	Ni	Cu	Zn	Ga	Ge	As	Se	Mo	Ag	Cd	In	Sn	Sb	Te	Au (ppb)	Hg	Tl	Pb	Bi	Au/Ag	Reference
FÅVNE																															
GS19-ROV10-R02	Sulfide ore, Cu-rich	0.10	23.30	23.70	35	<5	<10	<77	7.10	3779	<1	2.38 (%)	335	0.1	<5	0.1	0.4	2	1.8	1.3	0.7	2	0.2	0.01	34	<0.005	<0.02	4	1.9	0.02	this study
GS19-ROV10-R03	Sulfide ore, Cu-rich	0.04	11.40	29.40	13	<5	<10	<77	31.05	3060	<1	2.62 (%)	1215	0.6	<5	11	0.4	9	1.8	2.6	0.8	2	0.6	0.01	330	<0.005	<0.02	4	2.0	0.2	this study
GS19-ROV10-R04	Sulfide ore, Cu-rich	0.04	5.27	33.30	5.1	<5	<10	<77	36.37	4540	<1	5.60 (%)	500	0.4	<5	16	0.9	9	5.4	<0.5	2.3	2	0.6	0.01	709	<0.005	<0.02	3	6.5	0.1	this study
GS19-ROV10-R05	Sulfide ore, Cu-rich	0.03	0.06	48.40	1.8	<5	<10	<77	21.61	9780	<1	9.15 (%)	1540	0.9	<5	38	0.9	12	6.0	3.0	2.9	4	1.5	<0.01	1635	<0.005	<0.02	6	3.5	0.3	this study
GS20-ROV10-R01	Sulfide ore, Zn-rich	0.04	18.30	26.70	39	<5	<10	<77	8.95	233	1	1015	13.90 (%)	1.1	12	2.0	1.8	20	74	89	<0.005	20	7.4	0.01	24	0.09	0.2	197	<0.01	0.0003	this study
GS20-ROV10-R02a	Sulfide ore, Zn-rich	0.13	8.61	31.20	17	<5	<10	<77	10.11	1525	<1	2640	31.15 (%)	7.8	19	3.6	4.1	21	99	385	<0.005	93	20	0.01	48	0.04	0.04	189	0.01	0.0005	this study
GS20-ROV10-R02b	Sulfide ore, Zn-rich	0.15	12.90	30.10	13	<5	<10	<77	8.22	1080	<1	3260	29.17 (%)	11.2	12	2.6	3.2	14	95	408	<0.005	152	22	0.01	49	0.05	0.06	179	<0.01	0.0005	this study
GS20-ROV10-R02c	Sulfide ore, Zn-rich	0.06	14.01	29.40	10	<5	<10	<77	10.35	1010	<1	2390	23.40 (%)	7.5	12	2.6	2.7	21	70	285	0.01	106	13	0.02	54	0.03	0.07	191	<0.01	0.0008	this study
GS21-ROV07-R07-bottom	Sulfide ore, Cu-rich (base of chimney)	0.06	11.30	13.28	<100	–	–	10	29	3720	4	4.74 (%)	1.27 (%)	0.5	0.3	1	1.2	2	7.9	17	–	–	0.5	<0.01	558	<1	0.1	7	2.7	0.07	Sabina Strmić Palinkaš (unpub. data)
GS21-ROV07-R06-top	Sulfide ore, Zn-rich (top of chimney)	0.10	9.08	13.33	<100	–	–	66	12.7	1680	3	2340	25.80 (%)	9	1.6	13	0.05	18	63	351	–	–	17	<0.01	2.5	<1	0.05	127	0.1	0.00004	Sabina Strmić Palinkaš (unpub. data)
	Sulfide ore, Cu-rich (*n = 10*)	0.13	5.58	32.98	<100	–	<100	23	35.65	4517	3.2	6.38 (%)	0.35 (%)	0.9	0.4	8.2	0.7	4.2	4.8	2.8	–	–	0.9	<0.1	467	<1	<0.1	4.8	3.3	0.10	Norwegian Petroleum Directorate (2022)
	Sulfide ore, Zn-rich (*n = 3*)	0.99	1.40	25.33	<100	–	<100	167	33.30	1370	5.7	1.17 (%)	9.44 (%)	4.8	4.8	35	0.6	99	32	107	–	–	8.2	<0.1	164	<1	2.2	91	0.2	0.01	Norwegian Petroleum Directorate (2022)
LOKI'S CASTLE																															
GS17-ROV20-R07	Sulfide ore	5.82	0.06	31.30	637	<5	<10	232	21.26	368	<1	2.40 (%)	2.39 (%)	3.0	<5	56	340	2	48	75	0.1	9	5.7	17	219	2.1	2.9	6390	31	0.005	this study
GS17-ROV20-R09	Sulfide ore, oxidized	10.19	0.93	0.67	722	111	10	2943	32.66	54	2	1455	1075	3.5	<5	144	7.5	32	<0.5	0.9	0.03	1	0.6	0.9	31	0.5	0.3	231	2.5	–	this study
GS17-ROV20-R05-Core	Sulfide ore	4.07	<0.01	32.70	1105	<5	<10	155	29.93	10	<1	5610	5.17 (%)	1.4	<5	43	220	1	36	116	<0.005	9	31	13	135	0.7	1.2	1.08 (%)	1.9	0.004	this study

(*continued on next page*)

Table 2 (*continued*)

Sample ID	Rock type	Si (%)	Ca (%)	S (%)	Ba	V	Cr	Mn	Fe (%)	Co	Ni	Cu	Zn	Ga	Ge	As	Se	Mo	Ag	Cd	In	Sn	Sb	Te	Au (ppb)	Hg	Tl	Pb	Bi	Au/Ag	Reference
GS17-ROV20-R05-Cap	Barite-silica cap	29.82	0.48	7.77	13.21 (%)	9	<10	232	5.82	23	3	626	5220	2.6	<5	1220	12	28	89	6.6	0.01	2	137	1.8	3560	67	154	1560	0.1	0.04	this study
GS17-ROV20-R03	Sulfide ore	3.39	0.01	49.80	609	<5	<10	387	16.86	15	1	2.02 (%)	9.15 (%)	1.7	<5	65	790	2	31	273	0.1	4	5.0	26	245	0.6	0.8	1.19 (%)	11	0.01	this study
GS17-ROV20-R02-Core	Sulfide ore	9.40	0.01	40.80	1555	<5	<10	155	15.18	0.5	2	9180	5.58 (%)	2.4	<5	87	360	2	51	128	<0.005	18	38	19	326	2.5	3.6	2.17 (%)	6.2	0.01	this study
GS17-ROV20-R02-Cap	Barite-silica cap	25.24	0.14	11.35	13.52 (%)	11	<10	155	5.20	5.0	3	1850	1.38 (%)	2.8	<5	798	69	17	45	30	<0.005	10	52	4.0	1665	11	27	3590	1.1	0.04	this study
	Sulfide ores (W mound; *n = 15*)	11.41	9.42	13.00	3693	9.5	3.7	–	9.67	19	2.2	5372	9079	4.0	1.5	64	137	6.6	11	30	<0.1	3.7	8.2	–	315	5.0	2.7	1527	5.1	0.03	da Cruz (2015)
	Sulfide ores (E mound; *n = 7*)	17.10	4.61	14.31	4451	18	3.2	–	10.44	3.1	3.0	5993	1.66 (%)	4.4	2.7	66	148	13	5.5	54	<0.1	6.6	4.6	–	266	2.9	0.8	1094	5.8	0.05	da Cruz (2015)
BASEMENT ROCKS																															
	Loki's Castle Sediments (*n = 22*)	24.09	4.54	0.10	455	164	96	1401	4.65	23	48	74	89	18	1.5	20	0.3	2	<0.5	<0.5	<0.1	2.8	0.8	–	0.8	<1	0.3	14	0.09	–	da Cruz (2015)
	Loki's Castle D-MORB (*n = 1*)	24.08	8.00	0.09	31	303	109	1495	7.89	45	61	72	71	17	1.8	4	<0.5	<2	<0.5	0.7	<0.1	<1	<0.1	–	<1	<1	<0.05	<5	<0.1	–	da Cruz (2015)
	Global MORB	23.60	8.23	0.11	17	250	326	1320	7.27	56	200	70	80	21	1.6	0.1	0.2	0.4	0.03	0.1	0.08	1.0	0.01	0.005	1.2	0.01	0.007	0.6	0.01	0.04	Arevalo & McDonough (2010)
	Upper mantle	22.20	3.89	0.02	13	110	1969	1029	6.18	91	1610	31	63	7	1.2	0.1	0.06	–	0.01	0.05	0.02	0.8	–	–	0.5	–	0.00002	0.3	0.01	0.05	Anderson (1989)
	Ultramafic rocks	21.80	2.40	0.0008	3	77	2500	1010	6.08	105	2110	15	60	4	1.1	–	0.02	0.06	0.003	0.03	0.002	0.5	0.005	–	0.5	–	0.00002	0.2	0.01	0.2	Anderson (1989)

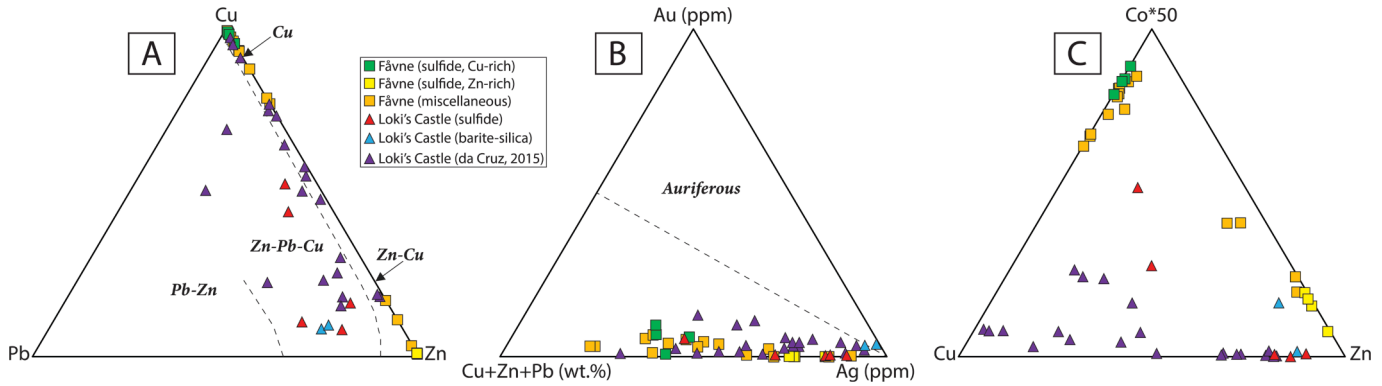

Fig. 4. Metal associations in samples from Fåvne and Loki's Castle based on whole-rock geochemical data. (**A**) Base metal classification including reference fields for different sub-types of VMS deposits (Galley et al., 2007). (**B**) Classification based on relative proportions of base metals (Cu, Zn, Pb) versus precious metals (Au, Ag). (**C**) Relationship between Co, Cu and Zn. Plotted miscellaneous data for Fåvne are from Norwegian Petroleum Directorate (2022) and Sabina Strmić Palinkaš (unpub. data).

2021). On the other hand, several elements that have been inferred as 'ultramafic markers', in particular Ni (≤1 ppm; Table 2), but also Se, Sn and Au, have low concentrations at Fåvne compared to global ultramafic-hosted deposits.

4.2.2. Loki's Castle

The analyzed samples from Loki's Castle are all chimney fragments from the western mound (n = 5; Table 2). Sulfide cores and barite-silica caps (Fig. 3a) in individual samples were analyzed separately. These new data complements a more extensive whole-rock geochemical dataset previously reported by da Cruz (2015) (summarized in Table 2).

The Loki's Castle samples show moderate to high Zn (up to 9.2 wt%), Cu (up to 2.4 wt%) and Pb (up to 2.2 wt%) concentrations in variable proportions, and mostly low but locally moderate Co concentrations (up to 368 ppm; Table 2; Fig. 4). In contrast to Fåvne, the concentrations of Cu and Zn are broadly positively correlated (Table 2; da Cruz, 2015). Gold and Ag concentrations reach 3.6 and 89 ppm, respectively, and Au: Ag ratios vary between 0.004 and 0.01. Other elements locally present in concentrations above 1000 ppm include Mn (in one extensively oxidized sample) and As; elements locally above 100 ppm include V, Se, Cd, Sb and Tl; and elements locally above 10 ppm include Cr, Mo, Sn, Te, Hg and Bi (Table 2). Both Si (up to 29.82 wt%) and Ba (up to 13.52 wt%) are primarily associated with the barite-silica caps, but high concentrations are also present in the sulfide cores (up to 9.40 wt% Si and 1555 ppm Ba; Table 2). Furthermore, the barite-silica caps are systematically enriched in As, Mo, Sb, Au, Hg and Tl, but depleted in Fe, Cu, Zn, Se, Cd, Sn, Te, Pb and Bi, relative to the sulfide cores (Table 2). Notably, Co shows no clear fractionation between the sulfide cores and the barite-silica caps.

The mineralogical–geochemical character of Loki's Castle is broadly similar to mafic-hosted SMS deposits globally (Hannington et al., 2005; Fouquet et al., 2010). However, several atypical features, most notably the enrichments in Ba, Pb and As (Table 2; Fig. 4), most likely reflect the sedimentary input at this field (Hannington et al., 1995; da Cruz, 2015; Baumberger et al., 2016a; Baumberger et al., 2016b).

4.3. Mineral chemistry

4.3.1. Pyrrhotite

Pyrrhotite from Cu-rich assemblages from Fåvne (Fig. 2c, e) is characterized by high average Co concentrations, between 6695 and 7693 ppm (up to 1.03 wt%; Table 3; Electronic Supplementary Material 3). Cobalt exhibits smooth downhole ablation profiles. Copper is also consistently present in high concentrations (average 1020 to 3496 ppm). Minor amounts of Mo (up to 10 ppm) and Bi (up to 1.7 ppm) are detected in a few of the analyses (Table 3; Electronic Supplementary Material 3).

In contrast, pyrrhotite from Loki's Castle (Fig. 3a-c) shows low Co concentrations (average from below detection limit to 58 ppm, up to 99 ppm), but moderate to high Cu (average 436 to 3425 ppm) and Se (average 861 to 1111 ppm) concentrations (Table 3; Electronic Supplementary Material 3). Lead (up to 80 ppm) is detected in several analyses. Locally elevated concentrations of Bi (up to 369 ppm), Te (173 ppm), Sb (up to 5.9 ppm), Tl (up to 5.6 ppm) and Ag (up to 2.3 ppm) may be related to Bi-Te-bearing and Sb-Tl-Ag-bearing microscopic inclusions.

4.3.2. Isocubanite

Isocubanite from Cu-rich assemblages from Fåvne (Fig. 2c, e) exhibits average Co concentrations between 4885 and 5295 ppm (up to 7141 ppm; Table 3; Electronic Supplementary Material 3). Cobalt shows smooth downhole profiles. All analyzed samples show similar concentrations of Zn (average 1466 to 1843 ppm), Ag (average 9.7 to 22 ppm) and In (average 5.8 to 10 ppm). Locally detected elements include Sn (up to 1219 ppm), Pb (up to 190 ppm), Cd (up to 79 ppm), Sb (up to 61 ppm), Mo (up to 45 ppm), Ga (up to 35 ppm), Bi (up to 34 ppm), As (up to 31 ppm), Au (up to 27 ppm) and Ge (up to 21 ppm; Table 3; Electronic Supplementary Material 3), some of which may in part be related to microscopic inclusions (Bi-Pb-Au and As-Mo, respectively). Notably, the highest concentrations of Zn, Ga, Ge, Cd, Sn, Sb and Pb are all associated with isocubanite grains that show textural evidence of having replaced sphalerite, suggesting that this element suite may in part have been inherited from sphalerite (cf., Rottier et al., 2016).

Isocubanite from Loki's Castle (Fig. 3b-d) exhibits average Co concentrations ranging from below detection limit to 119 ppm (up to 152 ppm; Table 3; Electronic Supplementary Material 3). All analyzed samples show very high average Zn concentrations, between 1.87 and 2.17 wt%, and similar average concentrations of Se (432 to 466 ppm), Mn (214 to 244 ppm), Cd (53 to 98 ppm), Ag (56 ppm), Te (21 ppm) and Bi (0.1 to 0.4 ppm). Lead (up to 1968 ppm) and Sn (up to 230 ppm) are only detected in one of the samples (Table 3; Electronic Supplementary Material 3). Locally elevated As (up to 225 ppm), Tl (up to 104 ppm) and Sb (up to 20 ppm) concentrations are likely related to microscopic Pb-As-Tl-Sb-bearing inclusions.

4.3.3. Pyrite

Pyrite grains from Loki's Castle (Fig. 3d) do not show any detectable Co; however, neither does isocubanite in the single sample analyzed (Table 3; Electronic Supplementary Material 3). Pyrite exhibits average concentrations of 295 ppm Cu, 236 ppm Se, 126 ppm Pb, 45 ppm Mn, 12 ppm Zn, 6.7 ppm Tl, 1.4 ppm Ag, 0.6 ppm Te, 0.6 ppm As and 0.1 ppm Sb (Table 3; Electronic Supplementary Material 3).

4.3.4. Sphalerite

Sphalerite from Cu-rich and Zn-rich assemblages from Fåvne

Table 3
Summary of mineral chemical data for Fåvne and Loki's Castle. Data marked with '*' were obtained by WDS; all other data were obtained by LA-ICP-MS. The data are reported in parts per million (1 ppm = 1 mg/kg) unless noted otherwise. Elements marked with '–' are below the limit of detection. The raw data are available in Electronic Supplementary Materials 2 and 3.

Mineral/ Sample ID	Sample type		V	Cr	Mn	Fe (%)	Co	Ni	Cu	Zn	Ga	Ge	As	Se	Mo	Ag	Cd	In	Sn	Sb	Te	Au	Hg	Tl	Pb	Bi
FÅVNE																										
Pyrrhotite																										
GS19-ROV10-R03 (Section A)	Sulfide ore, Cu-rich	mean	–	–	–	60.21*	7650	–	1020	–	–	–	–	–	–	–	–	–	–	–	–	–	–	–	–	–
n = 9		max	–	–	–	*61.04**	*8944*	–	*2182*	–	–	–	–	–	–	–	–	–	–	–	–	–	–	–	–	–
		min	–	–	–	*59.73**	*6362*	–	*525*	–	–	–	–	–	–	–	–	–	–	–	–	–	–	–	–	–
GS19-ROV10-R03 (Section D)	Sulfide ore, Cu-rich	mean	–	–	–	61.92*	6695	–	1217	–	–	–	–	–	1.5	–	–	–	–	–	–	–	–	–	–	0.05
n = 15		max	–	–	–	*62.40**	*8552*	–	*1705*	–	–	–	–	–	*10*	–	–	–	–	–	–	–	–	–	–	*0.7*
		min	–	–	–	*61.10**	*5829*	–	*727*	–	–	–	–	–	–	–	–	–	–	–	–	–	–	–	–	–
GS19-ROV10-R04 (Section A)	Sulfide ore, Cu-rich	mean	–	–	–	61.30*	7331	–	1962	–	–	–	–	–	–	–	–	–	–	–	–	–	–	–	–	–
n = 7		max	–	–	–	*61.78**	*1.03 (%)*	–	*2871*	–	–	–	–	–	–	–	–	–	–	–	–	–	–	–	–	–
		min	–	–	–	*60.40**	*5257*	–	*482*	–	–	–	–	–	–	–	–	–	–	–	–	–	–	–	–	–
GS19-ROV10-R04 (Section E)	Sulfide ore, Cu-rich	mean	–	–	–	60.64*	7693	–	3496	–	–	–	–	–	2.0	–	–	–	–	–	–	–	–	–	–	0.2
n = 29		max	–	–	–	*60.93**	*1.01 (%)*	–	*9063*	–	–	–	–	–	*8.7*	–	–	–	–	–	–	–	–	–	–	*1.7*
		min	–	–	–	*60.19**	*4587*	–	*1480*	–	–	–	–	–	–	–	–	–	–	–	–	–	–	–	–	–
Isocubanite																										
GS19-ROV10-R03 (Section D)	Sulfide ore, Cu-rich	mean	–	–	–	42.38*	5148	–	21.44 (%)*	1466	–	–	2.2	–	3.8	15	–	5.8	11	–	–	0.2	–	–	1.5	4.9
n = 14		max	–	–	–	*43.06**	*5714*	–	*21.79 (%)**	*1716*	–	–	*31*	–	*45*	*18*	–	*9.6*	*48*	–	–	*2.1*	–	–	*9.9*	*34*
		min	–	–	–	*41.87**	*4438*	–	*21.04 (%)**	*1273*	–	–	–	–	–	*12*	–	*3.3*	–	–	–	–	–	–	–	–
GS19-ROV10-R04 (Section A)	Sulfide ore, Cu-rich	mean	–	–	–	42.62*	4885	–	21.45 (%)*	1555	–	–	–	–	–	11	–	7.8	–	–	–	–	–	–	–	–
n = 10		max	–	–	–	*43.22**	*5131*	–	*21.79 (%)**	*1886*	–	–	–	–	–	*12*	–	*10*	–	–	–	–	–	–	–	–
		min	–	–	–	*41.87**	*4685*	–	*21.04 (%)**	*1381*	–	–	–	–	–	*9.6*	–	*6.5*	–	–	–	–	–	–	–	–
GS19-ROV10-R04 (Section E)	Sulfide ore, Cu-rich	mean	–	–	–	43.37*	5295	–	20.50 (%)*	1720	1.8	1.2	–	–	–	22	7.6	10	110	3.4	–	0.9	–	–	9.2	1.3
n = 29		max	–	–	–	*43.92**	*7141*	–	*20.97 (%)**	*3375*	*35*	*21*	–	–	–	*27*	*79*	*15*	*1219*	*61*	–	*19*	–	–	*190*	*10*
		min	–	–	–	*42.90**	*3561*	–	*19.88 (%)**	*1319*	–	–	–	–	–	*14*	–	*3.8*	–	–	–	–	–	–	–	–
GS19-ROV10-R05	Sulfide ore, Cu-rich	mean	–	–	–	43.14*	4962	–	20.96 (%)*	1843	–	–	–	–	–	9.7	–	8.0	–	–	–	1.6	–	–	0.9	1.1
n = 17		max	–	–	–	*43.72**	*5901*	–	*21.27 (%)**	*2557*	–	–	–	–	–	*13*	–	*11*	–	–	–	*27*	–	–	*7.6*	*6.4*
		min	–	–	–	*42.70**	*4245*	–		*1504*	–	–	–	–	–	*7.4*	–	*5.3*	–	–	–	–	–	–	–	–

(*continued on next page*)

Table 3 (*continued*)

Mineral/ Sample ID	Sample type		V	Cr	Mn	Fe (%)	Co	Ni	Cu	Zn	Ga	Ge	As	Se	Mo	Ag	Cd	In	Sn	Sb	Te	Au	Hg	Tl	Pb	Bi
									*20.18 (%)**																	
Sphalerite																										
GS19-ROV10-R03 (Section A)	Sulfide ore, Cu-rich	mean	–	–	36	7.71	751	–	3323	N/A	24	31	–	–	0.1	34	1553	1.0	349	60	–	–	8.7	–	300	–
n = 14		max	–	–	*56*	*10.60*	*1417*	–	*6007*	*N/A*	*40*	*52*	–	–	*2.1*	*87*	*2122*	*1.4*	*474*	*98*	–	–	*12*	–	*613*	–
		min	–	–	*22*	*4.19*	*389*	–	*1800*	*N/A*	*14*	*9.8*	–	–	–	*11*	*1090*	*0.6*	*226*	*38*	–	–	*5.6*	–	*37*	–
GS19-ROV11-R14	Sulfide ore, Zn-rich	mean	–	–	38	10.40	112	–	1160	N/A	40	21	2.8	–	–	3.7	1345	2.3	1008	136	–	–	9.4	–	13	–
n = 21		max	–	–	*54*	*14.36*	*182*	–	*2805*	*N/A*	*185*	*34*	*9.5*	–	–	*7.2*	*2728*	*7.0*	*3082*	*382*	–	–	*12*	–	*38*	–
		min	–	–	*23*	*6.28*	*70*	–	*141*	*N/A*	–	*9.8*	–	–	–	–	*102*	–	–	*8.5*	–	–	*7.6*	–	–	–
GS20-ROV10-R02b	Sulfide ore, Zn-rich	mean	–	–	46	9.24	647	–	4349	N/A	11	35	0.3	–	0.9	129	1060	0.6	241	62	–	–	20	–	952	–
n = 15		max	–	–	*83*	*12.56*	*1529*	–	*6900*	*N/A*	*28*	*57*	*1.0*	–	*3.6*	*385*	*1889*	*2.0*	*794*	*115*	–	–	*24*	–	*3594*	–
		min	–	–	–	*6.63*	*263*	–	*955*		*5.3*	*18*	–	–	–	*10*	*621*	*0.08*	*30*	*27*	–	–	*15*	–	*37*	–
GS20-ROV10-R01	Sulfide ore, Zn-rich	mean	–	–	53	14.01	414	–	3911	N/A	2.2	49	0.5	–	6.5	249	698	0.2	75	46	–	–	20	0	1124	0
n = 15		max	–	–	*89*	*18.07*	*607*	–	*1.23 (%)*	*N/A*	*4.3*	*121*	*5.6*	–	*32*	*544*	*1288*	*0.5*	*193*	*108*	–	–	*70*	*0.1*	*5472*	*0.05*
		min	–	–	–	*10.65*	*235*	–	*1688*	*N/A*	–	*18*	–	–	*0.5*	*33*	*147*	–	–	*15*	–	–	*11*	–	*49*	–
Magnetite																										
GS19-ROV10-R04 (Section A)	Sulfide ore, Cu-rich	mean	–	–	–	N/A	93	–	–	–	–	–	–	–	4.6	–	–	–	–	–	–	–	–	–	–	–
n = 13		max	–	–	–	*N/A*	*112*	–	–	–	–	–	–	–	*16*	–	–	–	–	–	–	–	–	–	–	–
		min	–	–	–	–	*32*	–	–	–	–	–	–	–	–	–	–	–	–	–	–	–	–	–	–	–
LOKI'S CASTLE																										
Pyrrhotite																										
GS17-ROV17-R01	Sulfide ore (W mound)	mean	–	–	–	61.48*	58	–	3425	–	–	–	–	861	–	–	–	–	–	–	18	–	–	–	1.1	31
n = 18		max	–	–	–	*62.30**	*99*	–	*4406*	–	–	–	–	*1517*	–	–	–	–	–	–	*173*	–	–	–	*9.0*	*369*
		min	–	–	–	*60.71**	*30*	–	*1605*	–	–	–	–	*195*	–	–	–	–	–	–	–	–	–	–	–	–
GS17-ROV20-R05	Sulfide ore (W mound)	mean	–	–	–	61.23*	–	–	436	–	–	–	–	1111	–	0.1	–	–	–	0.3	7.3	–	–	0.3	9.4	0.4
n = 20		max	–	–	–	*62.29**	–	–	*1044*	–	–	–	–	*2830*	–	*2.3*	–	–	–	*5.9*	*70*	–	–	*5.6*	*80*	*4.5*
		min	–	–	–	*60.49**	–	–	*143*	–	–	–	–	*354*	–	–	–	–	–	–	–	–	–	–	–	–
Isocubanite																										
GS17-ROV17-R01	Sulfide ore (W mound)	mean	–	–	214	41.25*	119	–	21.71 (%)*	2.17 (%)	–	–	–	466	–	56	98	–	–	–	21	–	–	–	–	0.1
n = 20		max	–	–	*286*	*42.22**	*152*	–	*22.79 (%)**	*3.15 (%)*	–	–	–	*782*	–	*69*	*150*	–	–	–	*44*	–	–	–	–	*0.9*
		min	–	–	*155*	*40.38**	*75*	–	*20.71 (%)**	*1.73 (%)*	–	–	–	*282*	–	*43*	*75*	–	–	–	–	–	–	–	–	–
GS17-ROV20-R10	Sulfide ore (W mound)	mean	–	–	244	42.56*	–	–	20.75 (%)*	1.87 (%)	–	–	45	432	–	56	53	–	119	1.3	21	–	–	19	201	0.4

(*continued on next page*)

Table 3 (*continued*)

Mineral/ Sample ID	Sample type		V	Cr	Mn	Fe (%)	Co	Ni	Cu	Zn	Ga	Ge	As	Se	Mo	Ag	Cd	In	Sn	Sb	Te	Au	Hg	Tl	Pb	Bi
n = 16		max	–	–	*458*	*43.05**	–	–	*21.23 (%)**	*2.75 (%)*	–	–	*225*	*1683*	–	*86*	*101*	–	*230*	*20*	*65*	–	–	*104*	*1968*	*5.0*
		min	–	–	–	*41.78**	–	–	*20.24 (%)**	*1.23 (%)*	–	–	–	*155*	–	*39*	*38*	–	*75*	–	–	–	–	–	*2.3*	–
Pyrite																										
GS17-ROV20-R10	Sulfide ore (W mound)	mean	–	–	45	47.29*	–	–	295	12	–	–	0.6	236	–	1.4	–	–	–	0.1	0.6	–	–	6.7	126	–
n = 29		max	–	–	*307*	*47.62**	–	–	*1490*	*47*	–	–	*5.6*	*569*	–	*4.9*	–	–	–	*1.8*	*14*	–	–	*88*	*437*	–
		min	–	–	–	*46.79**	–	–	–	–	–	–	–	*46*	–	–	–	–	–	–	–	–	–	*0.03*	*0.7*	–
Sphalerite																										
GS17-ROV17-R01	Sulfide ore (W mound)	mean	–	–	2287	13.97	129	–	277	N/A	0.9	–	–	339	–	0.5	2457	0.1	17	–	10	–	6.3	–	–	–
n = 22		max	–	–	*2853*	*16.70*	*148*	–	*472*	*N/A*	*8.3*	–	–	*453*	–	*0.7*	*2733*	*0.9*	*174*	–	*25*	–	*8.0*	–	–	–
		min	–	–	*1924*	*10.99*	*105*	–	*145*	*N/A*	–	–	–	*228*	–	*0.4*	*2106*	–	–	–	*2.5*	–	*4.7*	–	–	–
GS17-ROV20-R05	Sulfide ore (W mound)	mean	–	–	413	16.29	–	–	398	N/A	1.4	–	–	465	–	1.0	2706	0.2	107	0.1	28	–	6.3	–	1.3	0.04
n = 21		max	–	–	*547*	*22.96*	–	–	*1577*	*N/A*	*8.8*	–	–	*781*	–	*2.6*	*3406*	*2.3*	*824*	*1.8*	*92*	–	*11*	–	*11*	*0.5*
		min	–	–	*345*	*13.62*	–	–	*166*	*N/A*	–	–	–	*247*	–	*0.5*	*1973*	–	–	–	*5.8*	–	*4.2*	–	–	–

(Fig. 2d) shows average Co concentrations between 112 and 751 ppm (up to 1529 ppm) and average Fe concentrations between 7.71 and 14.01 wt% (Table 3; Electronic Supplementary Material 2; Electronic Supplementary Material 3). All analyzed samples exhibit variable average concentrations of Cu (1160 to 4349 ppm), Cd (698 to 1553 ppm), Pb (13 to 1124 ppm), Sn (75 to 1008 ppm), Ag (3.7 to 249 ppm), Sb (46 to 136 ppm), Mn (36 to 53 ppm), Ge (21 to 49 ppm), Ga (2.2 to 40 ppm), Hg (8.7 to 20 ppm) and In (0.2 to 2.3 ppm). Molybdenum (up to 32 ppm) and As (up to 9.5 ppm) are only detected locally (Table 3; Electronic Supplementary Material 3). All of the above-mentioned elements generally show smooth downhole signals.

Sphalerite from Loki's Castle (Fig. 3b-d) shows average Co concentrations from below detection limit to 129 ppm (up to 148 ppm) and average Fe concentrations between 13.97 and 16.29 wt% (Table 3; Electronic Supplementary Material 2; Electronic Supplementary Material 3). The overall higher sphalerite Fe concentrations at Loki's Castle relative to Fåvne are consistent with the sedimentary input at this site (Keith et al., 2014). Sphalerite grains in both of the analyzed samples exhibit similar average concentrations of Cd (2457 to 2706 ppm), Mn (413 to 2287 ppm), Se (339 to 465 ppm), Cu (277 to 398 ppm), Sn (17 to 107 ppm), Te (10 to 28 ppm), Hg (6.3 ppm), Ga (0.9 to 1.4 ppm) and Ag (0.5 to 1.0 ppm). Lead (up to 11 ppm), Sb (up to 1.8 ppm) and Bi (up to 0.5 ppm) are detected in a small number of analyses and are likely related to microscopic Pb-Sb-Bi-bearing inclusions.

4.3.5. Magnetite

Semi-quantitative analyses of magnetite from a Cu-rich assemblage from Fåvne reveal moderate Co concentrations (~100 ppm) and low Mo concentrations (~10 ppm) in all analyzed grains (Table 3; Electronic Supplementary Material 3). Both Co and Mo show smooth downhole profiles.

4.4. Trace element mapping

Trace element mapping was performed across intergrown pyrrhotite and isocubanite from a Cu-rich assemblage from Fåvne (Fig. 5). The results show that Zn, Ag, In and Sn preferentially partition into isocubanite and that these elements are evenly distributed within the mineral, albeit a weak zonation is observed for In. The signals for Co indicate that it occurs in similar concentrations in pyrrhotite and isocubanite and that it is evenly distributed within each mineral (Fig. 5). The high Cu concentrations in pyrrhotite, as observed in spot data, are seemingly masked in the map due to the presence of isocubanite (>20 wt % Cu; Table 3). The signals for As, Mo, Sb, Au, Pb and Bi are overall low in both pyrrhotite and isocubanite. However, locally increased signals for these and for several of the previously discussed elements (Zn, Ag, In, Sn, Cu and Co) are visible along fractures, vugs and grain boundaries in the mapped area. These highly localized element enrichments can likely be explained by microscopic to sub-microscopic coatings of sulfides or sulfosalts along the fracture surfaces. Bismuth in particular shows a clear spatial association with chalcopyrite fracture coatings visible in the associated photomicrograph (Fig. 5). These results support the interpretation that local enrichments in As, Mo, Sb, Au, Pb and Bi detected during spot analyses may in part be caused by microscopic inclusions (Table 3; Electronic Supplementary Material 3).

5. Discussion

5.1. Mineralogical distribution of Co

Our petrographic study accompanied by LA-ICP-MS spot analyses and mapping reveal that Co is predominantly hosted in Fe-, Cu-Fe- and Zn-sulfides at both Fåvne and Loki's Castle. Additionally, preliminary data indicate moderate Co concentrations in Fåvne magnetite (~100 ppm; Table 3) and a more comprehensive chemical characterization of Fe-oxides and Fe-oxyhydroxides from this deposit is thus warranted. The

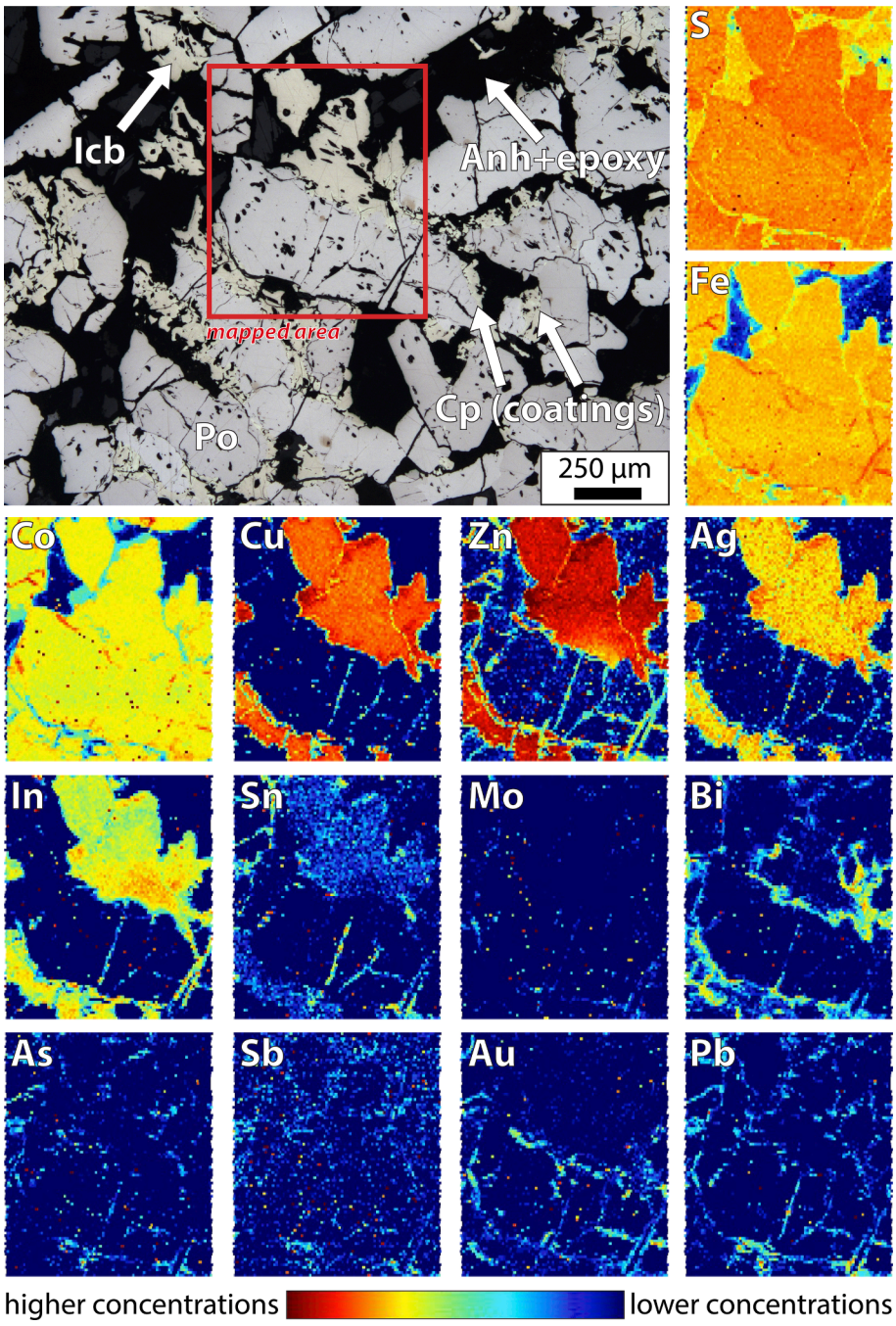

Fig. 5. LA-ICP-MS element maps for an assemblage comprising pyrrhotite, isocubanite and chalcopyrite (in delicate coatings along fractures and grain boundaries in isocubanite) from Fåvne. Scales are in counts per second; absolute values vary between different elements. See text for details. Abbreviations: Anh – anhydrite; Cp – chalcopyrite; Icb – isocubanite; Po – pyrrhotite.

smooth downhole ablation profiles for Co in all the analyzed minerals suggest that it is present as evenly distributed, lattice-bound substitutions that can be attributed to simple exchange of Co^{2+} for Fe^{2+} or Zn^{2+} (Vaughan and Rosso, 2006; Cook et al., 2009; Maslennikov et al., 2009). Such incorporation of Co is limited by crystal-chemical controls and particularly important is the compatibility of spin states between Co^{2+} and the divalent cation in a specific lattice (Vaughan and Craig, 1978; Bajwah et al., 1987). Previous studies have indicated that such controls may impart partitioning of Co between co-crystallized minerals (generally arsenopyrite > pyrite > pyrrhotite, sphalerite > chalcopyrite > magnetite; Gavelin and Gabrielson, 1947; Hawley and Nichol, 1961; Arnold et al., 1962; Vaughan and Craig, 1978; Vaughan, 1979; Mookherjee and Philip, 1979; Bajwah et al., 1987; Dare et al., 2011, 2012; George et al., 2016; Xu et al., 2021). Such partitioning of Co was not resolvable in our element maps of inferred co-crystallized pyrrhotite and isocubanite from Fåvne (Fig. 5), but spot data indicate a weak preference of Co for pyrrhotite ($D_{Po/Icb}$ = 1.3–1.5, calculated using average Co concentrations in 3 samples from Table 3). None of the other analyzed minerals from the AMOR assemblages crystallized together in equilibrium, inhibiting further assessment of Co partitioning between competing minerals. The overall distribution of Co that we observe (pyrrhotite > isocubanite > sphalerite > magnetite at Fåvne, isocubanite ≈ sphalerite > pyrrhotite at Loki's Castle; Table 3) also reflects changing hydrothermal fluid conditions during mineral formation (e.g., temperature; see Section 5.2.1).

In contrast to the studied Fåvne assemblages, similarly Co-rich ores

Table 4
Compilation of geologic and fluid data for selected examples of the key types of hydrothermal Co deposits globally.

Deposit type	Deposit/ district	Cobalt resource[1]	Presence of mafic–ultramafic rocks	Fluid NaCl[2]	Fluid temperature[3]	Comment
ACTIVE SYSTEMS						
Seafloor massive sulfide Cu(-Zn-Pb-Au-Ag-Co) deposits						
	Fåvne, Arctic Mid-Ocean Ridge	Avg. ~ 0.3 % Co in samples	Stratigraphic footwall is dominated by mafic ± ultramafic rocks	4.2–8.0 (FI)	197–332 °C (FI)	Primary FI in anhydrite. Mixing with cold seawater indicated.
	Rainbow, Mid-Atlantic Ridge	Avg. ~ 0.5 % Co in samples	Stratigraphic footwall is dominated by ultramafic and local mafic rocks	4.4 (DM); 4.1–8.5 (FI)	360–365 °C (DM); 160–370 °C (FI)	Direct measurements and primary FI in anhydrite
	Ashadze-1, Mid-Atlantic Ridge	Avg. ~ 0.3 % Co in samples	Stratigraphic footwall is dominated by ultramafic and local mafic rocks	3.6 (DM); 5–7.8 (FI)	355 °C (DM); 235–355 °C (FI)	Direct measurements and primary FI in anhydrite
Brine pool-related, stratiform Cu-Zn-Mn(–Co-Ag-Au) deposits						
	Atlantis II Deep, Red Sea	~90 Mt at 0.006 % Co	Stratigraphic footwall comprises mafic rocks overlain by evaporite-bearing sediments	~26 (DM); 19–32 (FI)	66 °C (DM); ~400 °C (FI)	Direct measurements (Lower Brine) and primary FI in anhydrite (vent fluid)
FOSSIL SYSTEMS						
Volcanogenic massive sulfide Cu(-Zn-Pb-Au-Ag-Co) deposits						
	Windy Craggy, Canada	297 Mt at 0.07 % Co	Stratigraphic footwall comprises interbedded basalt and argillite	9–17	220–380 °C	Primary FI in quartz
	Ishkinino, Russia	~1 Mt at 0.2 % Co	The deposit occurs within a fault-bounded ultramafic body	7.1	150–200 °C (uncorr.)	Primary FI in calcite (high-T population)
	Küre, Turkey	13.3 Mt at 0.3 % Co + 29 Mt at 0.56 % Co (Aşıköy-Bakibaba + Mağaradoruk ore bodies)	Stratigraphic footwall is dominated by mafic rocks	0.9–5 (?)	162–317 °C (uncorr.)	FI of unclear paragenesis in quartz. Some data may reflect post-ore fluids.
	Northern Apennines District, Italy	Avg. 0.0026–0.31 % Co in samples from different ore bodies	Stratigraphic footwall is dominated by mafic and ultramafic rocks	2.6–9.3	120–360 °C (uncorr.)	Primary FI in quartz (main ore stage)
Sedimentary rock-hosted deposits, including stratabound Cu-(Co) deposits and 'Mississippi Valley Type' Pb-Zn(-Cu-Ag-Co) deposits						
	Mindola-Nkana, ZCB, Zambia	656 Mt at 0.065 % Co	Mafic intrusions are locally abundant in the basement in the western ZCB	37–54 (wt. % NaCl + KCl)	206–292 °C (uncorr.)	Primary FI in quartz and dolomite
	Kamoto, CCB, DR Congo	139.4 Mt at 0.35 % Co	Mafic-ultramafic complexes underlie the Co-rich northern part of the CCB	35–40 → 12–20	270–320 °C → 115–220 °C	Primary FI in quartz. Two ore stages (609 and 520 Ma).
	Luiswishi, CCB, DR Congo	8 Mt at 1.1 % Co		39–46	300–385 °C	Primary FI in quartz
	Walford Creek, Australia	40.9 Mt at 0.12 % Co	Mafic rocks are locally abundant in the stratigraphic footwall	6–7 → ~25 → ~30	>180 °C → 150–170 °C → 125 °C	Primary FI in quartz and sphalerite. Three ore stages.
	Ruby Creek (Bornite), USA	182.4 Mt at 0.019 % Co	Only minor mafic rocks in the stratigraphic footwall	4–13	120–225 °C	Primary FI in carbonates
	Mount Isa, Australia	182 Mt at 0.05 % Co (Cu ore body)	Voluminous mafic rocks in the stratigraphic footwall	10–20 (early) → 4–9 (late)	~270–350 °C	Primary FI in quartz that bracket Cu(–Co) ore
	Black Butte (Sheep Creek), USA	11.6 Mt at 0.1 % Co	The deposit is hosted in shale. Voluminous mafic–ultramafic rocks are unknown in the area.	~15 (?)	94–350 °C (uncorr.)	FI of unclear paragenesis in barite, quartz, sphalerite and carbonates
	Southeast Missouri Lead District, USA	Variable. Avg. grade 0.2 % Co in Mine La Motte – Fredericktown subdistrict.	Voluminous mafic–ultramafic intrusions to the south of the district, along the fluid flow path	5–35	~80–150 °C	Primary and secondary FI in sphalerite, quartz and dolomite
Metasedimentary rock-hosted Co-Cu-Au deposits						
	Blackbird District, USA	16.8 Mt at 0.74 % Co (district)	Mafic intrusions occur distal (>1 km) to ore bodies. Also voluminous mafic rocks deep in the stratigraphic footwall.	>35 (?)	250–350 °C (uncorr.)	FI of unclear paragenesis in quartz
	Cobalt Hill, Canada	Avg. ~ 0.6 % Co in samples	Mafic intrusions outcrop distal (~1 km) to the deposit, and have been inferred to occur in the stratigraphic footwall	26–46	~400 °C	Primary FI in quartz
	Juomasuo, Finland	5 Mt at 0.13 % Co	Ore bodies occur near contacts between the metasedimentary host rocks and ultramafic sills	28–30 (pre) → 5–20 (post)	>400 °C (pre) → 100–210 °C (post; uncorr.)	Primary FI in albite and secondary FI in quartz that pre- and post-date Co ore, respectively
'Five-element' (Ag-Ni-Co-As-Bi) and other Co-rich vein deposits						
	Cobalt-Gowganda District, Canada	~2 Mt at 1 % Co (district)	Veins occur in close to intermediate spatial association with mafic sills and sulfide-rich metavolcanic rocks	5–26	290–350 °C	Primary FI in quartz, calcite and axinite. Mixing with a low-salinity fluid indicated.
	McAra, Canada	72 kt at 1.27 % Co	Veins are hosted in mafic rocks interbedded with VMS-bearing siliciclastic sediments	15–25	133–235 °C (uncorr.)	Primary FI in quartz
	Bou Azzer, Morocco	5.7 Mt at 1.5 % Co (district)	Veins occur along tectonized contacts between a serpentinite body and diorite intrusions or evaporite-bearing volcano-sedimentary rocks	37–49 (wt. % NaCl + $CaCl_2$)	200–220 °C	Primary and secondary FI in quartz

(*continued on next page*)

Table 4 (*continued*)

Deposit type	Deposit/ district	Cobalt resource[1]	Presence of mafic–ultramafic rocks	Fluid NaCl[2]	Fluid temperature[3]	Comment
Fe(-Cu-Co) skarn deposits						
	Cihai, China	~100 Mt at 0.09 % Co	The skarn ores are principally hosted in mafic intrusive rocks	8–16 → 0.2–23	220–456 °C → 128–367 °C (uncorr.)	Primary FI in quartz, calcite and epidote. Two ore stages. Mixing with a low-salinity fluid indicated.
Fe-oxide – Cu-Au(-Ag-U-REE-Bi-Co) deposits						
	NICO, Canada	33 Mt at 0.11 % Co	Mafic rocks are locally abundant deep in the stratigraphic footwall	>32 (pre) → 17–37 (post)	>400 °C (est. from mineral stabilities)	(Pseudo)secondary FI in quartz and calcite that pre- and postdate Co ore. Temperature estimate is for Co ore stage.
	Ernest Henry, Australia	166 Mt at 0.05 % Co	Mafic rocks are subordinate in the district	30–70	250–600 °C (uncorr.)	Primary FI in quartz
	Guelb Moghrein, Mauritania	23.7 Mt at 0.014 % Co	The deposit is hosted in metacarbonate rocks enclosed by mafic-dominated metavolcanic rocks	0–25	380–440 °C	Secondary FI in carbonates. Mixing with a low-salinity fluid indicated.

[1]The listed Co resources are variably well defined, ranging from industry-compliant resources to preliminary or historic estimates. See references for details.
[2]Expressed as wt.% NaCl in zero-Mg endmember hydrothermal fluid (direct measurements) or wt.% NaCl equivalent (fluid inclusion data), unless noted otherwise.
[3]Temperatures from fluid inclusions reflect pressure-corrected homogenization temperatures, unless noted otherwise.
Abbreviations: CCB – Congolese Copperbelt; DM – direct measurement; est. – estimated; FI – fluid inclusions; Mt – million metric tonnes; VMS – volcanogenic massive sulfide; uncorr. – uncorrected; ZCB – Zambian Copperbelt.
References: Fåvne (this study); Rainbow (Douville et al., 2002; Charlou et al., 2002; Bortnikov et al., 2004; Fouquet et al., 2010); Ashadze-1 (Charlou et al., 2002; Bortnikov et al., 2010; Fouquet et al., 2010); Atlantis II Deep (Guney et al., 1988; Ramboz et al., 1988; Hannington et al., 2005, and references therein); Windy Craggy (Peter and Scott, 1999); Ishkinino (Melekestseva et al., 2013, and references therein; Slack et al., 2017, and references therein); Küre (Akbulut et al., 2016, and references therein); Northern Apennines District (Zaccarini and Garuti, 2008; Kiss et al., 2021) Mindola-Nkana (Slack et al., 2017, and references therein; Davey et al., 2021); Kamoto (El Desouky et al., 2009; Taylor et al., 2013; Saintilan et al., 2018); Luiswishi (El Desouky et al., 2009; Taylor et al., 2013); Walford Creek (Rohrlach et al., 1998; Aeon Metals, 2020); Ruby Creek (Hitzman, 1986; Trilogy Metals, 2019); Mount Isa (Heinrich et al., 1989, 1995; Slack et al., 2017, and references therein); Black Butte (Graham et al., 2012, and references therein; Slack et al., 2017, and references therein); Southeast Missouri Lead District (Gregg and Shelton, 1989, and references therein; Horrall et al., 1993; Seeger, 2008); Blackbird District (Nash and Hahn, 1989; Landis and Hofstra, 2012; Slack, 2012; Saintilan et al., 2017); Cobalt Hill (Schandl, 2004); Juomasuo (Vanhanen, 2001; Vasilopoulos et al., 2016; Slack et al., 2017, and references therein); Cobalt-Gowganda (Marshall et al., 1993; Slack et al., 2017, and references therein); McAra (Lindsay, 2020; Hendrickson, 2020); Bou Azzer (Essarraj et al., 2005; Slack et al., 2017, and references therein); Cihai (Tang et al., 2012; Hou et al., 2013; Zheng et al., 2017); NICO (Acosta, 2014; Acosta-Góngora et al., 2015); Ernest Henry (Kendrick et al., 2007; Slack et al., 2017, and references therein); Guelb Moghrein (Kolb et al., 2010).

from the Rainbow, Ashadze-1 and Logatchev-1 deposits along the Mid-Atlantic Ridge contain a variety of Co-sulfides, sulfarsenides and arsenides including cobaltpentlandite [$(Co,Ni,Fe)_9S_8$], cobaltite (CoAsS), linnaeite (Co_3S_4), minerals of the loellingite–safflorite series ($FeAs_2$ – $CoAs_2$), and Co-rich millerite [(Ni,Co)S] (Mozgova et al., 1999, 2008; Bogdanov et al., 2002; Lein et al., 2003; Fouquet et al., 2010). Notably, sulfide ores from these deposits generally have concentrations of As, Sb and Ni that are one to two orders of magnitude higher than those at Fåvne (Table 2; cf., Fouquet et al., 2010), whereas vent fluids at all four deposits have similarly low H_2S concentrations (<2 mM; Charlou et al., 2002; Charlou et al., 2010; Douville et al., 2002; Fouquet et al., 2010; Pedersen et al., 2021). As has been argued for hydrothermal Co mineralization in other geologic settings (cf., Jansson and Liu, 2020; Vasyukova and Williams-Jones, 2022), an increased availability of As, Sb and Ni together with Co at H_2S-limited conditions could explain the localized formation of discrete Co-minerals at deposits such as Rainbow, Ashadze-1 and Logatchev-1. In contrast, a distinctly lower As-Sb-Ni:H_2S ratio during mineral formation at Fåvne is consistent with the more extensive sequestration of Co in Fe-, Cu-Fe- and Zn-sulfides.

5.2. *Some genetic aspects of Co in SMS deposits*

Due to limited and biased (dominantly surficial) sampling it is generally difficult to assess and compare the metal endowments of SMS deposits (Petersen et al., 2016). With this in mind, it can however be observed that the average Co concentrations in sulfide ores from global SMS deposits typically range from a few up to hundreds of ppm, such as at Loki's Castle, whereas high average concentrations are only known from a few examples (0.3–0.5 wt% Co at Fåvne, Rainbow and Ashadze-1; Table 4; Hannington et al., 2005; Fouquet et al., 2010; Toffolo et al., 2020; this study).

Differences in the capacity of the hydrothermal fluid to mobilize and transport Co is likely a key cause of this variability (Fouquet et al., 2010). Data for natural seafloor hydrothermal fluids (Trefry et al., 1994; Metz and Trefry, 2000) and results from experiments and thermodynamic modelling (Susak and Crerar, 1985; Liu et al., 2011; Migdisov et al., 2011; Brugger et al., 2016; Jansson and Liu, 2020; Williams-Jones and Vasyukova, 2022) indicate that Co solubility increases with increasing fluid temperature, salinity and fO_2, and decreasing pH. Furthermore, the composition of the stratigraphic footwall influences the availability of leachable Co (e.g., ~105 ppm Co in ultramafic rocks, ~56 ppm in MORB, ~19 ppm in shale, ~3 ppm in felsic rocks; Anderson, 1989; Arevalo and McDonough, 2010; Hitzman et al., 2017), the chemistry of the hydrothermal fluid, and the deposit morphology (Hannington et al., 1995; Fouquet et al., 2010).

At the scale of individual SMS deposits, the sensitivity of Co solubility to temperature is commonly manifested in the enrichment of Co in high-temperature Cu-rich over low-temperature Zn-rich assemblages (Fig. 4c; Hannington et al., 1995; Fouquet et al., 1998, 2010; Toffolo et al. 2020). Furthermore, Co has been observed to be enriched during replacement of low-temperature by high-temperature sulfide assemblages (i.e., hydrothermal maturation) and to be largely immobile during so-called zone-refining processes (Fouquet et al., 1996; 1998; Maslennikov et al., 2009; Grant et al., 2018; Toffolo et al., 2020). Due to its affinity for high-temperature and mature sulfides, the spatial zonation of Co in SMS deposits is thus controlled by the geometry of high-temperature fluid flow and venting, the fluid mixing–cooling history, and the degree of reworking.

Some of these genetic aspects are discussed in more detail below based on a comparison of Fåvne and Loki's Castle with comparable SMS and VMS deposits globally.

5.2.1. *Influence of stratigraphic footwall composition on Co enrichment and zonation*

The Co-rich SMS deposits documented thus far globally seem to form within ultramafic-hosted (Rainbow and Ashadze-1) and suspected

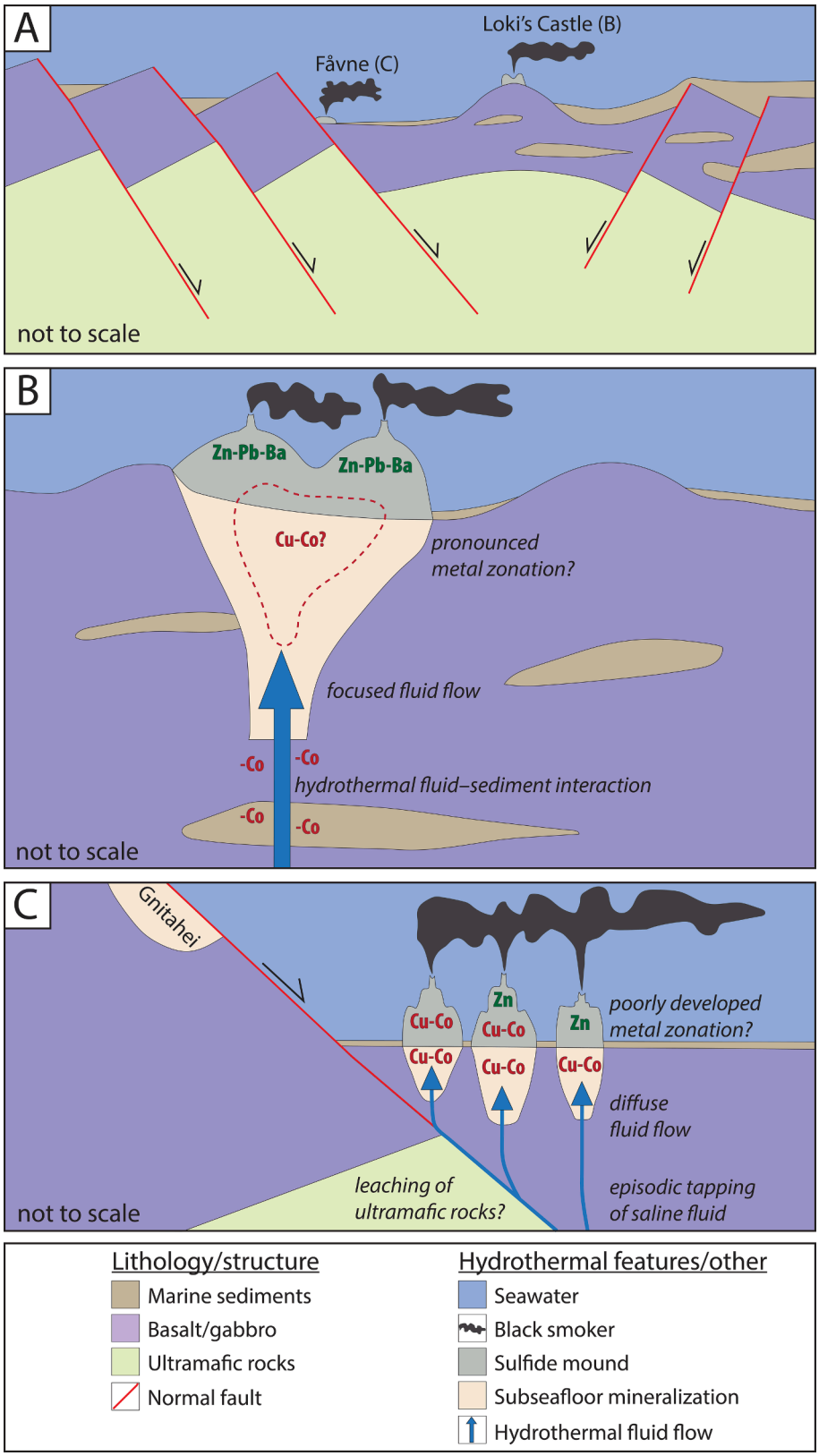

Fig. 6. Conceptual genetic model for Fåvne and Loki's Castle, integrating available geological, mineralogical and geochemical data and observations (Pedersen et al., 2010a; Baumberger et al., 2016a; Baumberger et al., 2016b; Stenløkk et al., 2019; Brekke et al., 2021; this study). Different factors controlling the enrichment and the zonation of Co in the two deposits are highlighted (see text for detailed discussion). (**A**) Composite cross section of the northern Mohns Ridge showing the distinct settings of Fåvne and Loki's Castle. (**B**) Close-up of Loki's Castle. (**C**) Close-up of Fåvne.

ultramafic-influenced (Fåvne) hydrothermal systems (Fouquet et al., 2010; this study). This could mean that ultramafic-hosted systems are generally more efficient in mobilizing and concentrating Co than mafic-hosted as well as felsic-hosted (arc-related) systems, potentially due to the increased Co concentrations in ultramafic rocks and/or their distinct fluid chemistries (Fouquet et al., 2010; Patten et al., 2022). However, in fossil onshore VMS deposits that have been subjected to more detailed exploration, high and locally exploitable Co grades have been found in both ultramafic-hosted and mafic-hosted deposits in a range of tectonic settings (e.g., Deerni, China; Ishkinino and Ivanovskoe, Russia; Küre,

Turkey; Løkken, Norway; Sambagawa Belt, Japan; Windy Craggy and Kona, Canada; Outokumpu District, Finland; Northern Apennines District, Italy; Table 4; Kase and Yamamoto, 1988; Peter et al., 2007; Peltonen et al., 2008; Slack et al., 2017; Petavratzi et al., 2019; Horn et al., 2021; Patten et al., 2022). Furthermore, thermodynamic modelling of high-temperature seawater–peridotite and seawater–basalt interaction indicated no major differences in the accumulation of Co in the hydrothermal fluid (Fig. 5 of Toffolo et al., 2020).

Mafic-hosted and ultramafic-hosted SMS deposits have been noted to generally exhibit distinct morphologies and mineralogical-chemical zonation patterns (Fouquet et al., 2010). In this context, mafic-hosted SMS deposits are commonly characterized by focused high-temperature venting, a well-developed conical mound and, with maturity, pronounced mineralogical-chemical zonation, such that Co is concentrated in the mound interior and the stockwork (e.g., TAG, Mid-Atlantic Ridge; Fouquet et al., 1996, 1998, 2010; Grant et al., 2018). The same Co zonation has been observed in mafic-hosted VMS deposits preserved in ophiolites (e.g., Skouriotissa, Cyprus; Keith et al., 2016). By analogy with such deposits, more Cu-Co-rich sulfides might thus occur in the interior of the large Loki's Castle mound (Fig. 6b), which has also been suggested from gravity coring (Pedersen et al., 2010a; da Cruz, 2015). In contrast, ultramafic-hosted SMS deposits are commonly characterized by more diffuse high-temperature discharge as a result of the more permeable basement rocks. These deposits therefore tend to be distinctly flatter and exhibit less pronounced mineralogical-chemical zonation, such that Co and other high-temperature elements are more widespread across the surface of the deposit (e.g., Rainbow and Ashadze-1; Marques et al., 2006; Fouquet et al., 2010). Similar enrichment of Co in surficial relative to deeper ore bodies has also been noted in some ultramafic-hosted VMS deposits (e.g., Northern Apennines District, Italy; Zaccarini, and Garuti, 2008). While the presence and role of ultramafic rocks at Fåvne are currently poorly understood, the similar diffuse style of high-temperature venting at this deposit may thus partly explain the high Co concentrations in the surficial sulfides (Fig. 6c). More detailed investigation at both Fåvne and Loki's Castle is now required to verify these aspects. Globally, the apparently increased Co concentrations in ores from ultramafic-hosted relative to mafic-hosted SMS deposits may thus in part reflect a sampling bias, related to the predominance of surface sampling in SMS exploration and the typical Co zonation in the two deposit types (Co at the surface versus Co in the core; Hannington et al., 2005; Fouquet et al., 2010; Toffolo et al., 2020).

In the case of Loki's Castle and some other modern SMS deposits forming in sedimented settings (e.g., Guaymas Basin; Von Damm et al., 1985), hydrothermal fluid–sediment interaction elevates the fluid pH to values that are distinctly higher than those typical of Co-rich systems (5.5–6 at Loki's Castle versus ~ 3 at Rainbow and Ashadze-1; Charlou et al., 2002; Charlou et al., 2010; Douville et al., 2002; Baumberger et al., 2016b). This should decrease the capacity of the Loki's Castle fluids to transport Co and other pH-sensitive metals (Fig. 6b; cf., Hannington et al., 1995; Jansson and Liu, 2020) and adds a further explanation for the overall Co-poor character of this deposit. Notably however, several Co-rich VMS deposits occur in sediment-bearing mafic–ultramafic sequences (e.g., Windy Craggy; Table 4; Peter and Scott, 1999), suggesting that the presence of sediments is not always detrimental to Co mineralization.

5.2.2. *Potential importance of high-salinity fluids for Co mineralization*

Most types of hydrothermal Co deposits globally form from high-salinity brines that facilitate efficient transport of Co as Co-Cl complexes (Table 4; Susak and Crerar, 1985; Metz and Trefry, 2000; Liu et al., 2011; Migdisov et al., 2011; Brugger et al., 2016; Vasyukova and Williams-Jones, 2022). The comparatively low salinities of seafloor hydrothermal systems (seawater ≈ 3.2 wt% NaCl, typical range ≈ 0.2–8 wt% NaCl; Von Damm, 1995) have therefore been inferred as one of the fundamental reasons for the scarcity of Co-rich SMS deposits (Metz and Trefry, 2000). The Loki's Castle vent fluids are slightly depleted in Cl relative to seawater (average ~ 2.9 wt% NaCl; Baumberger et al., 2016b), whereas the Co-rich Ashadze-1 and Rainbow deposits discharged weakly to moderately Cl-enriched fluids during recent measurements (3.6 and 4.4 wt% NaCl, respectively; Table 4; Charlou et al., 2002; Charlou et al., 2010; Douville et al., 2002). Fluid inclusion data for anhydrite intergrown with pyrrhotite-isocubanite in the Cu-Co-rich assemblages from Fåvne (Fig. 3a) indicate precipitation from saline and hot hydrothermal fluids that mixed with cold seawater (4.2–8.0 wt% NaCl eq. and up to > 330 °C; Table 4; Electronic Supplementary Material 1). Similar brines have also been documented via fluid inclusions at Rainbow (4.1–8.5 wt% NaCl eq.; Bortnikov et al., 2004) and Ashadze-1 (5–7.8 wt% NaCl eq.; Bortnikov et al., 2010). They have also been documented at the large-tonnage, low-grade Atlantis II Deep stratiform deposit, Red Sea (19–32 wt% NaCl eq.; Table 4; Ramboz et al., 1988) as well as at several Co-rich VMS deposits (9–17 wt% NaCl eq. at Windy Craggy in Canada, 7.1 wt% NaCl eq. at Ishkinino in Russia, 2.6–9.3 wt% NaCl eq. at Northern Apennines District in Italy; Table 4; Peter and Scott, 1999; Melekestseva et al., 2013, and references therein; Kiss et al., 2021) whereas their involvement is ambiguous at others (0.9–5 wt% NaCl eq. at Küre, Turkey; Table 4; Akbulut et al., 2016).

In some tectonic settings, such high-salinity brines may be explained by influx of magmatic fluid (e.g., Windy Craggy; Table 4; Peter and Scott, 1999; Schmidt et al., 2021), leaching of evaporite strata (e.g., Atlantis II Deep; Table 4; Ramboz et al., 1988) or dewatering of sedimentary pore fluids (Tornos and Heinrich, 2008). However, at mid-ocean ridges such as the AMOR, they can most likely be attributed to phase separation under high-pressure, supercritical conditions, leading to the accumulation of a high-salinity liquid at depth (Von Damm, 1990, 1995; Butterfield and Massoth, 1994; Hannington et al., 1995; Von Damm et al., 1997; Coumou et al., 2009). Such deep-seated brines may then be periodically tapped during the evolution of a SMS deposit, leading to sharp temporal variations in hydrothermal fluid chlorinity and metal content, and consequently, in the composition of the hydrothermal precipitates (Hannington et al., 1995). There is thus evidence for saline fluids with enhanced capacity to mobilize and transport Co being present, at least intermittently, during the formation of Fåvne (Fig. 6c) and several similar Co-rich deposits elsewhere and such fluids may have been important for their Co endowment, warranting further investigation.

6. Concluding remarks and future directions

In this study, we characterized ore assemblages from the active Fåvne and Loki's Castle SMS deposits, Arctic Mid-Ocean Ridges, and investigated the mineralogical distribution and some genetic aspects of Co. Samples from the two deposits show considerable variation in whole-rock Co concentrations (average ~ 0.3 wt% Co at Fåvne and < 100 ppm Co at Loki's Castle), similar to the variations observed between SMS deposits at a global scale. Due to simple $Co^{2+} \leftrightarrow (Fe,Zn)^{2+}$ substitutions, Co is incorporated in Fe-, Cu-Fe- and Zn-sulfides and to a lesser degree in Fe-oxides in these deposits, and its mineralogical distribution reflects both crystal-chemical controls (e.g., spin state compatibility between Co^{2+} and the divalent cation) and changing hydrothermal fluid conditions (e.g., temperature) during mineral formation. Low fluid As-Sb-Ni:H_2S ratios likely inhibit the formation of discrete Co-minerals at Fåvne. At Loki's Castle, we suggest that more Co-rich sulfides might occur in the interior of the deposit. Nevertheless, the elevated hydrothermal fluid pH values due to interaction with sediments are likely detrimental to the overall transport and mineralization of Co in this system (Fig. 6b). We find evidence suggesting that saline fluids with enhanced capacity to mobilize and transport Co may have been important for the Co endowment at Fåvne (Fig. 6c) and several similar Co-rich SMS and VMS deposits globally (Table 4). While it is unclear whether ultramafic basement rocks provide any increased extraction of Co compared to mafic rocks (Toffolo et al., 2020), such rocks can facilitate 'diffuse' high-temperature venting that concentrates Co in the

surficial parts of the sulfide deposits (e.g., Rainbow and Ashadze-1; Fouquet et al., 2010). A similar scenario may be applicable to Fåvne (Fig. 6c). Ultramafic-hosted SMS deposits chiefly develop in association with low-angle detachment faults at magma-starved segments of slow- and ultraslow-spreading mid-ocean ridges as well as in ocean–continent transition and supra-subduction zone settings (McCaig et al., 2007; Escartín et al., 2008; Fouquet et al., 2010; Pedersen et al., 2010b; Sauter et al., 2013; Morris et al., 2017; Patten et al., 2022). In the case of the AMOR, such tectonic features appear to be most prominent from the central Mohns Ridge and northwards (Fig. 6a; Pedersen et al., 2010b). Here, dredging and plume surveys have indicated strong potential for several additional, likely ultramafic-hosted SMS deposits that may contain Co mineralization similar to that found at Fåvne (Snow et al., 2001, Edmonds et al., 2003; Connelly et al., 2007; Upchurch et al., 2007; Pedersen et al., 2010b).

More broadly, our observations from active SMS deposits together with the compiled data for key types of hydrothermal Co deposits globally (Table 4) highlight the general importance of high-salinity fluids and mafic–ultramafic rocks for Co mineralization (cf., Vasyukova and Williams-Jones, 2022). While genetic models for the different deposit types included in Table 4 vary markedly, it can be observed that the highest Co grades commonly develop where highly saline fluids are in intimate contact with mafic–ultramafic rocks (e.g., 1.5 wt% Co at the Bou Azzer vein deposit, Morocco; Essarraj et al., 2005). Furthermore, Co mineralization in several deposit types that do not universally contain significant Co, such as in some sedimentary rock-hosted, stratabound Cu deposits in the Central African Copper Belt or in some 'Mississippi Valley Type' Pb-Zn deposits in the Southeast Missouri Lead District, USA, has been attributed to interaction between typical high-salinity ore-forming brines and locally occurring mafic–ultramafic rocks (Table 4; Annels and Simmonds, 1984; Horrall et al., 1993; Hitzman et al., 2017; Saintilan et al., 2018; Vasyukova and Williams-Jones, 2022). Conversely, in some SMS and VMS deposits where mafic–ultramafic rocks are ubiquitous, high Co concentrations can at least in part be explained by unusually saline fluids relative to seawater (Table 4). Furthermore, overprinting of such VMS deposits by later high-salinity fluids such as basinal brines can lead to remobilization of Co and the formation of high Co grade vein mineralization (e.g., McAra deposit, Canada; Table 4; Hendrickson, 2020). Our findings thus reinforce that evidence for interaction between high-salinity fluids and mafic–ultramafic rocks (and their contained sulfide deposits) should be considered a key exploration criterion in the intensifying global search for new hydrothermal Co deposits.

Similar to what has previously been done for other metals (e.g., Au; Hannington et al., 1999), comprehensive studies aiming to document and link the distribution of Co in modern SMS and ancient VMS deposits across a range of scales (i.e., mineral grain to global-scale) are suggested as an important avenue of future research that could lead to improved resource assessments. Additionally, new insights from field-, analytical-, experimental- and modelling-based investigations into the processes and conditions that are conducive for Co mineralization at the seafloor and during subsequent geologic events (e.g., Jansson and Liu, 2020; Hendrickson, 2020) will aid both deep-sea and onshore exploration for this critical metal.

Declaration of Competing Interest

The authors declare that they have no known competing financial interests or personal relationships that could have appeared to influence the work reported in this paper.

Data availability

Data will be made available on request.

Acknowledgements

This research was funded by Equinor (Akademiaavtale project A31687) and by the Centre for Deep Sea Research, University of Bergen. Trine Dahl and Irina Dumitru helped with sample preparation and Glenn Bark, Mathis Warlo and Tom-Ivar Eilertsen provided assistance during the SEM analytical work. We further thank Sean McClenaghan for performing the LA-ICP-MS trace element mapping at Trinity College Dublin, Dieter Garbe-Schønberg for providing the Aljustrel-2 standard pellet prepared at Kiel University, and Jeff Hedenquist and Antonio Arribas for helpful comments on an earlier version of Table 4. On the part of *Ore Geology Reviews*, we gratefully acknowledge Rémi Coltat and one anonymous reviewer for their constructive and stimulating reviews and Lisard Torró for excellent editorial handling.

Appendix A. Supplementary data

Supplementary data to this article can be found online at https://doi.org/10.1016/j.oregeorev.2022.105261.

References

Acosta, P., 2014. Origins and geochemical characterization of the iron-oxide-copper-gold deposits in the Great Bear magmatic zone, NWT, Canada. University of Alberta. PhD Thesis,.

Acosta-Góngora, P., Gleeson, S.A., Samson, I.M., Corriveau, L., Ootes, L., Taylor, B.E., Creaser, R.A., Muehlenbachs, K., 2015. Genesis of the Paleoproterozoic NICO iron oxide–cobalt–gold–bismuth deposit, Northwest Territories, Canada: evidence from isotope geochemistry and fluid inclusions. Precambrian Res. 268, 168–193.

Aeon Metals. (2020). *Walford Creek resource update*. Available at: https://www.aeonmetals.com.au/wp-content/uploads/2020/02/2019-Walford-Creek-Resource-Update-17Dec19-Final.pdf [Accessed 30th January 2021].

Akbulut, M., Oyman, T., Cicek, M., Selby, D., Özgenç, İ., Tokcaer, M., 2016. Petrography, mineral chemistry, fluid inclusion microthermometry and Re–Os geochronology of the Küre volcanogenic massive sulfide deposit (Central Pontides, Northern Turkey). Ore Geol. Rev. 76, 1–18.

ALS. (2021). 2021 ALS geochemistry fee schedule. Available at: https://www.alsglobal.com/myals/downloads [Accessed 4th March 2021].

Alves Dias, P., Blagoeva, D., Pavel, C. and Arvanitidis, N. (2018). *Cobalt: demand-supply balances in the transition to electric mobility*. Science for Policy Report 112285. Luxembourg: European Commission, Joint Research Centre.

Anderson, D.L., 1989. Composition of the Earth. Science 243, 367–370.

Annels, A.E., Simmonds, J.R., 1984. Cobalt in the Zambian copperbelt. Precambrian Res. 25, 75–98.

Arevalo, R., McDonough, W.F., 2010. Chemical variations and regional diversity observed in MORB. Chem. Geol. 271, 70–85.

Arnold, R.G., Coleman, R.G., Fryklund, V.C., 1962. Temperature of crystallization of pyrrhotite and sphalerite from the Highland-Surprise Mine, Coeur D'Alene District. Idaho. Econ. Geol. 57, 1163–1174.

Bajwah, Z., Seccombe, P., Offler, R., 1987. Trace element distribution Co: Ni ratios and genesis of the Big Cadia iron-copper deposit, New South Wales. Australia. Miner. Depos. 22, 292–300.

Banza Lubaba Nkulu, C., Nawrot, T.S., Haufroid, V., Decrée, S., De Putter, T., Smolders, E., Ilunga Kabyla, B., Numbi Luboya, O., Ndala Ilunga, A., Mwanza Mutombo, A. and Nemery, B. (2009). High human exposure to cobalt and other metals in Katanga, a mining area of the Democratic Republic of Congo. Environ. Res. 109, 745–752.

Banza Lubaba Nkulu, C., Casas, L., Haufroid, V. De Putter, T., Saenen, N.D., Kayembe-Kitenge, T., Musa Obadia, P., Kyanika Wa Mukoma, D., Lunda Ilunga, J-M., Nawrot, T.S., Luboya Numbi, O., Smolders, E. and Nemery, B. (2018). Sustainability of artisanal mining of cobalt in DR Congo. Nat. Sustain. 1, 495–504.

Baumberger, T., Früh-Green, G.L., Dini, A., Boschi, C., van Zuilen, K., Thorseth, I.H., Pedersen, R.B., 2016a. Constraints on the sedimentary input into the Loki's Castle hydrothermal system (AMOR) from B isotope data. Chem. Geol. 443, 111–120.

Baumberger, T., Früh-Green, G.L., Thorseth, I.H., Lilley, M.D., Hamelin, C., Bernasconi, S.M., Okland, I.E., Pedersen, R.B., 2016b. Fluid composition of the sediment-influenced Loki's castle vent field at the ultra-slow spreading Arctic Mid-Ocean Ridge. Geochim. Cosmochim. Acta 187, 156–178.

Belousov, I.A., Danyushevsky, L.V., Olin, P.H., Gilbert, S.E. and Thompson, J. (2015). STDGL3 - a new calibration standard for sulphide analysis by LA-ICP-MS. In: *Proceedings of the 2015 Goldschmidt Conference, 16–21 August 2015, Prague, Czech Republic*. Geochemical Society and the European Association of Geochemistry, abstract number 251.

Bogdanov, Yu.A., Bortnikov, N.S., Vikent'ev, I.V., Lein, A.Y., Gurvich, E.G., Sagalevich, A.M., Simonov, V.A., Ikorskii, S.V., Stavrova, O.O. and Apollonov, V.N. (2002). Mineralogical-geochemical peculiarities of hydrothermal sulfide ores and fluids in the Rainbow field associated with serpentinites, Mid-Atlantic Ridge (36°14'N). Geol. Ore Depos. 44, 444–473.

Bortnikov, N.S., Simonov, V.A., Bogdanov, Y.A., 2004. Fluid inclusions in minerals from modern sulfide edifices: physicochemical conditions of formation and evolution of fluids. Geol. Ore Depos. 46, 64–75.
Bortnikov, N.S., Simonov, V.A., Fouquet, Y., Amplieva, E.E., 2010. Phase separation of fluid in the Ashadze deep-sea modern submarine hydrothermal field (Mid-Atlantic Ridge, 12°58′N): results of fluid inclusion study and direct observations. Dokl. Earth Sci. 435, 1446–1449.
Brekke, H., Stenløkk, J., Eriksen, S.H, Bjørnstad, A., Sandstå, N.R., Solvi, K. and Schiager, P. (2021). Deep sea minerals on the Norwegian continental shelf – developments in exploration. In: *Proceedings of the 34th Geological Winter Meeting, 6–8 January 2021 (virtual)*. Trondheim: Geological Society of Norway, pp. 9.
Brugger, J., Liu, W., Etschmann, B., Mei, Y., Sherman, D.M., Testemale, D., 2016. A review of the coordination chemistry of hydrothermal systems, or do coordination changes make ore deposits? Chem. Geol. 447, 219–253.
Bruvoll, V., Breivik, A.J., Mjelde, R., Pedersen, R.B., 2009. Burial of the Mohn-Knipovich seafloor spreading ridge by the Bear Island Fan: time constraints on tectonic evolution from seismic stratigraphy. Tectonics 28, TC4001.
Butterfield, D.A., Massoth, G.J., 1994. Geochemistry of north Cleft segment vent fluids: temporal changes in chlorinity and their possible relation to recent volcanism. J. Geophys. Res. Solid Earth 99, 4951–4968.
Charlou, J.L., Donval, J.P., Fouquet, Y., Jean-Baptiste, P., Holm, N., 2002. Geochemistry of high H_2 and CH_4 vent fluids issuing from ultramafic rocks at the Rainbow hydrothermal field (36°14′N, MAR). Chem. Geol. 191, 345–359.
Charlou, J.L., Donval, J.P., Konn, C., Ondréas, H., Fouquet, Y., Jean-Baptiste, P. and Fourré, E. (2010). High production and fluxes of H_2 and CH_4 and evidence of abiotic hydrocarbon synthesis by serpentinization in ultramafic-hosted hydrothermal systems on the Mid-Atlantic Ridge. In: Rona, P.A., Devey, C.W., Dyment, J. and Murton, B.J. (Eds.) *Diversity of hydrothermal systems on slow spreading ocean ridges*. AGU Geophysical Monograph 188, pp. 265–296.
Choi, S.K., Pak, S.J., Kim, J., Park, J.-W., Son, S.-K., 2021. Gold and tin mineralisation in the ultramafic-hosted Cheoeum vent field, Central Indian Ridge. Miner. Depos. 56, 885–906.
Connelly, D.P., German, C.R., Asada, M., Okino, K., Egorov, A., Naganuma, T., Pimenov, N., Cherkashev, G., Tamaki, K., 2007. Hydrothermal activity on the ultra-slow spreading southern Knipovich Ridge. Geochem. Geophys. Geosystems 8, Q08013.
Cook, N.J., Ciobanu, C.L., Pring, A., Skinner, W., Shimizu, M., Danyushevsky, L., Saini-Eidukat, B., Melcher, F., 2009. Trace and minor elements in sphalerite: a LA-ICPMS study. Geochim. Cosmochim. Acta 73, 4761–4791.
Coumou, D., Driesner, T., Weis, P., Heinrich, C.A., 2009. Phase separation, brine formation, and salinity variation at black smoker hydrothermal systems. J. Geophys. Res. Solid Earth 114, B03212.
da Cruz, M.I.F.S. (2015). Mineralogy and geochemistry of contrasting hydrothermal systems on the Arctic Mid Ocean Ridge (AMOR): the Jan Mayen and Loki's Castle vent fields. PhD Thesis, Universidade de Lisboa.
Danyushevsky, L., Robinson, P., Gilbert, S., Norman, M., Large, R., McGoldrick, P., Shelley, M., 2011. Routine quantitative multi-element analysis of sulphide minerals by laser ablation ICP-MS: standard development and consideration of matrix effects. Geochem. Explor. Environ. Anal. 11, 51–60.
Dare, S.A., Barnes, S.J., Prichard, H.M., Fisher, P.C., 2011. Chalcophile and platinum-group element (PGE) concentrations in the sulfide minerals from the McCreedy East deposit, Sudbury, Canada, and the origin of PGE in pyrite. Miner. Depos. 46, 381–407.
Dare, S.A., Barnes, S.J., Beaudoin, G., 2012. Variation in trace element content of magnetite crystallized from a fractionating sulfide liquid, Sudbury, Canada: implications for provenance discrimination. Geochim. Cosmochim. Acta 88, 27–50.
Davey, J., Roberts, S., Wilkinson, J.J., 2021. Copper-and cobalt-rich, ultrapotassic bittern brines responsible for the formation of the Nkana-Mindola deposits, Zambian Copperbelt. Geology 49, 341–345.
Donaldson, J.D., Beyersmann, D.B., 2010. Cobalt and cobalt compounds. Ullmann's Encyclopedia of Industrial Chemistry. John Wiley & Sons, New York.
Douville, E., Charlou, J.L., Oelkers, E.H., Bienvenu, P., Jove Colon, C.F., Donval, J.P., Fouquet, Y., Prieur, D., Appriou, P., 2002. The Rainbow vent fluids (36°14′N, MAR): the influence of ultramafic rocks and phase separation on trace metal content in Mid-Atlantic Ridge hydrothermal fluids. Chem. Geol. 184, 37–48.
Edmonds, H.N., Michael, P.J., Baker, E.T., Connelly, D.P., Snow, J.E., Langmuir, C.H., Dick, H.J.B., Mühe, R., German, C.R., Graham, D.W., 2003. Discovery of abundant hydrothermal venting on the ultraslow-spreading Gakkel ridge in the Arctic Ocean. Nature 421, 252–256.
Eickmann, B., Thorseth, I.H., Peters, M., Strauss, H., Bröcker, M., Pedersen, R.B., 2014. Barite in hydrothermal environments as a recorder of subseafloor processes: a multiple-isotope study from the Loki's Castle vent field. Geobiology 12, 308–321.
El Desouky, H.A., Muchez, P., Cailteux, J., 2009. Two Cu–Co sulfide phases and contrasting fluid systems in the Katanga Copperbelt, Democratic Republic of Congo. Ore Geol. Rev. 36, 315–332.
Elkins, L.J., Hamelin, C., Blichert-Toft, J., Scott, S.R., Sims, K.W.W., Yeo, I.A., Devey, C. W., Pedersen, R.B., 2016. North Atlantic hotspot-ridge interaction near Jan Mayen Island. Geochem. Perspect. Lett. 2, 55–67.
Escartín, J., Smith, D.K., Cann, J., Schouten, H., Langmuir, C.H., Escrig, S., 2008. Central role of detachment faults in accretion of slow-spreading oceanic lithosphere. Nature 455, 790–794.
Essarraj, S., Boiron, M.-C., Cathelineau, M., Banks, D.A., Benharref, M., 2005. Penetration of surface-evaporated brines into the Proterozoic basement and deposition of Co and Ag at Bou Azzer (Morocco): evidence from fluid inclusions. J. African Earth Sci. 41, 25–39.
Firstova, A., Stepanova, T., Cherkashov, G., Goncharov, A., Babaeva, S., 2016. Composition and formation of gabbro-peridotite hosted seafloor massive sulfide deposits from the Ashadze-1 hydrothermal field. Mid-Atlantic Ridge. Minerals 6, 19.
Fouquet, Y., Henry, K., Knott, R. and Cambon, P. (1998). Geochemical section of the TAG hydrothermal mound. In: Herzig, P.M., Humphris, S.E., Miller, D.J. and Zierenberg, R.A. (Eds.) *Drilling an Active Hydrothermal System on a Sediment-Free Slow-Spreading Ridge*. Proceedings of the Ocean Drilling Program Scientific Results 158, pp. 363–387.
Fouquet, Y., Cambon, P., Etoubleau, J., Charlou, J.L., Ondréas, H., Barriga, F.J.A.S., Cherkashov, G., Semkova, T., Poroshina, I., Bohn, M., Donval, J.P., Henry, K., Murphy, P. and Rouxel, O. (2010). Geodiversity of hydrothermal processes along the Mid-Atlantic Ridge and ultramafic-hosted mineralization: a new type of oceanic Cu-Zn-Co-Au volcanogenic massive sulfide deposit. In: Rona, P.A., Devey, C.W., Dyment, J. and Murton, B.J. (Eds.) *Diversity of hydrothermal systems on slow spreading ocean ridges*. AGU Geophysical Monograph 188, pp. 321–367.
Fouquet, Y., Knott, R., Cambon, P., Fallick, A., Rickard, D., Desbruyeres, D., 1996. Formation of large sulfide mineral deposits along fast spreading ridges. Example from off-axial deposits at 12°43′N on the East Pacific Rise. Earth Planet. Sci. Lett. 144, 147–162.
Galley, A.G., Hannington, M.D. and Jonasson, I.R. (2007). Volcanogenic massive sulphide deposits. In: Goodfellow, W.D. (Ed.) *Mineral deposits of Canada: a synthesis of major deposit types, district metallogeny, the evolution of geological provinces and exploration methods*. Special Publication 5. St John's: Geological Association of Canada, Mineral Deposits Division, pp. 141–161.
Garbe-Schönberg, D., Müller, S., 2014. Nano-particulate pressed powder tablets for LA-ICP-MS. J. Anal. At. Spectrom. 29, 990–1000.
Gavelin, S., Gabrielson, O., 1947. Spectrochemical investigation of sulphide minerals from ores of Skellefte district. The significance of minor constituents for certain practical and theoretical problems of economic geology. Sver. Geol. Und. Ser. C 491.
Géli, L., Renard, V., Rommevaux, C., 1994. Ocean crust formation processes at very slow spreading centers: a model for the Mohns Ridge, near 72°N, based on magnetic, gravity, and seismic data. J. Geophys. Res. Solid Earth 99, 2995–3013.
George, L.L., Cook, N.J., Ciobanu, C.L., 2016. Partitioning of trace elements in co-crystallized sphalerite–galena–chalcopyrite hydrothermal ores. Ore Geol. Rev. 77, 97–116.
Graham, G., Hitzman, M.W., Zieg, J., 2012. Geologic setting, sedimentary architecture, and paragenesis of the Mesoproterozoic sediment-hosted Sheep Creek Cu-Co-Ag deposit, Helena Embayment. Montana. Econ. Geol. 107, 1115–1141.
Grant, H.L.J., Hannington, M.D., Petersen, S., Frische, M., Fuchs, S.H., 2018. Constraints on the behavior of trace elements in the actively-forming TAG deposit, Mid-Atlantic Ridge, based on LA-ICP-MS analyses of pyrite. Chem. Geol. 498, 45–71.
Gregg, J.M., Shelton, K.L., 1989. Geochemical and petrographic evidence for fluid sources and pathways during dolomitization and lead-zinc mineralization in southeast Missouri: a review. Carbon. Evaporit. 4, 153–175.
Gulley, A.L., McCullough, E.A., Shedd, K.B., 2019. China's domestic and foreign influence in the global cobalt supply chain. Resour. Policy 62, 317–323.
Guney, M., Al-Marhoun, M.A., Nawab, Z.A., 1988. Metalliferous sub-marine sediments of the Atlantis-II-Deep. Red Sea. CIM Bull. 81, 33–39.
Hannington, M.D., de Ronde, C.E.J., Petersen, S., 2005. Sea-floor tectonics and submarine hydrothermal systems. In: Hedenquist, J.W., Thompson, J.F.H., Goldfarb, R.J., Richards, J.P. (Eds.), Economic Geology One Hundredth Anniversary Volume. Society of Economic Geologists, Littleton, pp. 111–141.
Hannington, M.D., Jonasson, I.R., Herzig, P.M. and Petersen, S. (1995). Physical and chemical processes of seafloor mineralization at mid-ocean ridges. In: Humphris, S. E., Zierenberg, R.A., Mullineaux, L.S. and Thomson, R.E. (Eds.) *Seafloor hydrothermal systems: physical, chemical, biological, and geological interactions*. AGU Geophysical Monograph 91, pp. 115–157.
Hannington M.D., Poulsen K.H., Thompson J.F.H., Sillitoe R.H. (1999). Volcanogenic gold in the massive sulfide environment. In: Barrie, C.T. and Hannington, M.D. (Eds.) *Volcanic-associated massive sulfide deposits: processes and examples in modern and ancient settings*. Rev. Econ. Geol. 8, pp. 325–356.
Hawley, J.E., Nichol, I., 1961. Trace elements in pyrite, pyrrhotite and chalcopyrite of different ores. Econ. Geol. 56, 467–487.
Hein, J.R., Mizell, K., Koschinsky, A., Conrad, T.A., 2013. Deep-ocean mineral deposits as a source of critical metals for high-and green-technology applications: comparison with land-based resources. Ore Geol. Rev. 51, 1–14.
Heinrich, C.A., Andrew, A.S., Wilkins, R.W., Patterson, D.J., 1989. A fluid inclusion and stable isotope study of synmetamorphic copper ore formation at Mount Isa. Australia. Econ. Geol. 84, 529–550.
Heinrich, C.A., Bain, J.H.C., Mernagh, T.P., Wyborn, L.A.I., Andrew, A.S., Waring, C.L., 1995. Fluid and mass transfer during metabasalt alteration and copper mineralization at Mount Isa. Australia. Econ. Geol. 90, 705–730.
Hendrickson, M.D., 2020. Regional and local controls on Archean rock-hosted cobalt mineralization at the McAra deposit, southern Superior Province, Ontario. Canada. Can. J. Earth Sci. 57, 1447–1462.
Hitzman, M.W., 1986. Geology of the Ruby Creek copper deposit, southwestern Brooks Range. Alaska. Econ. Geol. 81, 1644–1674.
Hitzman, M.W., Bookstrom, A.A., Slack, J.F. and Zientek, M.L. (2017). *Cobalt: styles of deposits and the search for primary deposits*. U.S. Geological Survey Open-File Report 2017–1155.
Horn, S., Gunn, A.G., Petavratzi, E., Shaw, R.A., Eilu, P., Törmänen, T., Bjerkgård, T., Sandstad, J.S., Jonsson, E., Kountourelis, S., Wall, F., 2021. Cobalt resources in Europe and the potential for new discoveries. Ore Geol. Rev. 130, 103915.
Horrall, K.B., Hagni, R.D., Kisvarsanyi, G., 1993. Mafic and ultramafic plutons associated with the New Madrid rift complex; a possible major source of the copper-cobalt-nickel mineralization of Southeast Missouri. Econ. Geol. 88, 328–343.

Hou, T., Zhang, Z., Santosh, M., Encarnacion, J., Wang, M., 2013. The Cihai diabase in the Beishan region, NW China: isotope geochronology, geochemistry and implications for Cornwall-style iron mineralization. J. Asian Earth Sci. 70–71, 231–249.

Humphris, S.E., Herzig, P.M., Miller, D.J., Alt, J.C., Becker, K., Brown, D., Brügmann, G., Chiba, H., Fouquet, Y., Gemmell, J.B., Guerin, G., Hannington, M.D., Holm, N.G., Honnorez, J.J., Iturrino, G.J., Knott, R., Ludwig, R., Nakamura, K., Petersen, S., Reysenbach, A.-L., Rona, P.A., Smith, S., Sturz, A.A., Tivey, M.K., Zhao, X., 1995. The internal structure of an active sea-floor massive sulphide deposit. Nature 377, 713–716.

Jansson, N.F., Liu, W., 2020. Controls on cobalt and nickel distribution in hydrothermal sulphide deposits in Bergslagen, Sweden - constraints from solubility modelling. GFF 142, 87–95.

Kase, K., Yamamoto, M., 1988. Minerals and geochemical characteristics of ores from the Besshi-type deposits in the Sambagawa Belt. Japan. Min. Geol. 38, 203–214.

Keith, M., Haase, K.M., Schwarz-Schampera, U., Klemd, R., Petersen, S., Bach, W., 2014. Effects of temperature, sulfur, and oxygen fugacity on the composition of sphalerite from submarine hydrothermal vents. Geology 42, 699–702.

Keith, M., Haase, K.M., Klemd, R., Krumm, S., Strauss, H., 2016. Systematic variations of trace element and sulfur isotope compositions in pyrite with stratigraphic depth in the Skouriotissa volcanic-hosted massive sulfide deposit, Troodos ophiolite. Cyprus. Chem. Geol. 423, 7–18.

Kendrick, M.A., Mark, G., Phillips, D., 2007. Mid-crustal fluid mixing in a Proterozoic Fe oxide–Cu–Au deposit, Ernest Henry, Australia: evidence from Ar, Kr, Xe, Cl, Br, and I. Earth Planet. Sci. Lett. 256, 328–343.

Kiss, G.B., Bendő, Z., Garuti, G., Zaccarini, F., Király, E., Molnár, F., 2021. Reconstruction of hydrothermal processes in the Cyprus type Fe-Cu-Zn deposits of the Italian Northern Apennines: results of combined fluid inclusion microthermometry, SEM-CL imaging and trace element analyses by LA-ICP-MS. Minerals 11, 165.

Klingelhöfer, F., Geli, L., Matias, L., Steinsland, N., Mohr, J., 2000. Crustal structure of a super-slow spreading centre: a seismic refraction study of Mohns Ridge, 72° N. Geophys. J. Int. 141, 509–526.

Kodaira, S., Mjelde, R., Gunnarsson, K., Shiobara, H., Shimamura, H., 1998. Evolution of oceanic crust on the Kolbeinsey Ridge, north of Iceland, over the past 22 Myr. Terra Nova 10, 27–31.

Kolb, J., Meyer, F.M., Vennemann, T., Sindern, S., Prantl, S., Böttcher, M.E. and Sakellaris, G.A. (2010). Characteristics of hydrothermal fluids forming the Guelb Moghrein Fe oxide-Cu-Au-Co deposit, Mauritania: ore mineral chemistry, fluid inclusions and isotope geochemistry. In Porter, T.M. (Ed.) *Hydrothermal iron oxide copper-gold and related deposits: a global perspective, v. 4 - advances in the understanding of IOCG deposits*. Adelaide: PGC Publishing, pp. 553–572.

Landis, G.P., Hofstra, A.H., 2012. Ore genesis constraints on the Idaho cobalt belt from fluid inclusion gas, noble gas isotope, and ion ratio analyses. Econ. Geol. 107, 1189–1205.

Lein, A.Y., Cherkashev, G.A., Ul'yanov, A.A., Ul'yanova, N.V., Stepanova, T.V., Sagalevich, A.M., Bogdanov, Y.A., Gurvich, E.G., Torokhov, M.P., 2003. Mineralogy and geochemistry of sulfide ores from the Logatchev-2 and Rainbow fields: similar and distinctive features. Geochem. Int. 41, 271–294.

Liao, S., Tao, C., Li, H., Barriga, F.J.A.S., Liang, J., Yang, W., Yu, J., Zhu, C., 2018. Bulk geochemistry, sulfur isotope characteristics of the Yuhuang-1 hydrothermal field on the ultraslow-spreading Southwest Indian Ridge. Ore Geol. Rev. 96, 13–27.

Lindsay, D.H.M., 2020. 5-element vein ore genesis in the Cobalt Embayment, Ontario. Imperial College, London. MSc Thesis.

Liu, W., Borg, S.J., Testemale, D., Etschmann, B., Hazemann, J.-L., Brugger, J., 2011. Speciation and thermodynamic properties for cobalt chloride complexes in hydrothermal fluids at 35–440 °C and 600 bar: an in-situ XAS study. Geochim. Cosmochim. Acta 75, 1227–1248.

Manheim, F., 1986. Marine cobalt resources. Science 232, 600–608.

Marques, A.F.A., Barriga, F.J.A.S., Chavagnac, V., Fouquet, Y., 2006. Mineralogy, geochemistry, and Nd isotope composition of the Rainbow hydrothermal field, Mid-Atlantic Ridge. Miner. Depos. 41, 52–67.

Marques, A.F.A., Roerdink, D.L., Baumberger, T., de Ronde, C.E.J., Ditchburn, R.G., Denny, A., Thorseth, I.H., Okland, I., Lilley, M.D., Whitehouse, M.J., Pedersen, R.B., 2020. The Seven Sisters hydrothermal system: first record of shallow hybrid mineralization hosted in mafic volcaniclasts on the Arctic Mid-Ocean Ridge. Minerals 10, 439.

Marshall, D.D., Diamond, L.W., Skippen, G.B., 1993. Silver transport and deposition at Cobalt, Ontario, Canada; fluid inclusion evidence. Econ. Geol. 88, 837–854.

Maslennikov, V.V., Maslennikova, S.P., Large, R.R., Danyushevsky, L.V., 2009. Study of trace element zonation in vent chimneys from the Silurian Yaman-Kasy volcanic-hosted massive sulfide deposit (Southern Urals, Russia) using laser ablation-inductively coupled plasma mass spectrometry (LA-ICPMS). Econ. Geol. 104, 1111–1141.

McCaig, A.M., Cliff, R.A., Escartín, J., Fallick, A.E., MacLeod, C.J., 2007. Oceanic detachment faults focus very large volumes of black smoker fluids. Geology 35, 935–938.

Melekestseva, I.Y., Zaykov, V.V., Nimis, P., Tret'Yakov, G.A., Tessalina, S.G., 2013. Cu–(Ni–Co–Au)-bearing massive sulfide deposits associated with mafic–ultramafic rocks of the Main Urals Fault, South Urals: geological structures, ore textural and mineralogical features, comparison with modern analogs. Ore Geol. Rev. 52, 18–36.

Metz, S., Trefry, J.H., 2000. Chemical and mineralogical influences on concentrations of trace metals in hydrothermal fluids. Geochim. Cosmochim. Acta 64, 2267–2279.

Michael, P.J., Langmuir, C.H., Dick, H.J.B., Snow, J.E., Goldstein, S.L., Graham, D.W., Lehnert, K., Kurras, G., Jokat, W., Mühe, R., Edmonds, H.N., 2003. Magmatic and amagmatic seafloor generation at the ultraslow-spreading Gakkel ridge, Arctic Ocean. Nature 423, 956–961.

Migdisov, A.A., Zezin, D., Williams-Jones, A.E., 2011. An experimental study of cobalt (II) complexation in Cl^- and H_2S-bearing hydrothermal solutions. Geochim. Cosmochim. Acta 75, 4065–4079.

Mookherjee, A., Philip, R., 1979. Distribution of copper, cobalt and nickel in ores and host-rocks, Ingladhal, Karnataka. India. Miner. Depos. 14, 33–55.

Morris, A., Anderson, M.W., Omer, A., Maffione, M., Van Hinsbergen, D.J., 2017. Rapid fore-arc extension and detachment-mode spreading following subduction initiation. Earth Planet. Sci. Lett. 478, 76–88.

Mozgova, N.N., Efimov, A., Borodaev, Y.S., Krasnov, S.G., Cherkashov, G.A., Stepanova, T.V., Ashadze, A.M., 1999. Mineralogy and chemistry of massive sulfides from the Logatchev hydrothermal field (14°45'N Mid-Atlantic Ridge). Explor. Min. Geol. 8, 379–395.

Mozgova, N.N., Trubkin, N.V., Borodaev, Y.S., Cherkashev, G.A., Stepanova, T.V., Semkova, T.A., Uspenskaya, T.Y., 2008. Mineralogy of massive sulfides from the Ashadze hydrothermal field, 13°N, Mid-Atlantic Ridge. Can. Mineral. 46, 545–567.

Mudd, G.M., Weng, Z., Jowitt, S.M., Turnbull, I.D., Graedel, T.E., 2013. Quantifying the recoverable resources of by-product metals: the case of cobalt. Ore Geol. Rev. 55, 87–98.

Nash, J.T. and Hahn, G.A. (1989). Stratabound Co-Cu deposits and mafic volcaniclastic rocks in the Blackbird mining district, Lemhi County, Idaho. In: Boyle, R.W. et al. (Eds.) *Sediment-hosted stratiform copper deposits*. Geological Association of Canada Special Paper 36, pp. 339–356.

NOAA. (2020). *Arctic basemap layers*. Available at: https://www.arcgis.com/home/item.html?id=94f14eb0995e4bfc9d2439fc868345da [Accessed 30th January 2021].

Norwegian Petroleum Directorate (2022). *Analytical results related to deep sea sulfide deposits*. Available at: https://www.npd.no/fakta/nyheter/generelle-nyheter/2022/havbunnsmineraler-analysene-av-provene-er-tilgjengelige/ [Accessed 12th October 2022].

Paton, C., Hellstrom, J., Paul, B., Woodhead, J., Hergt, J., 2011. Iolite: freeware for the visualisation and processing of mass spectrometric data. J. Anal. At. Spectrom. 26, 2508–2518.

Patten, C.G.C., Coltat, R., Junge, M., Peillod, A., Ulrich, M., Manatschal, G., Kolb, J., 2022. Ultramafic-hosted volcanogenic massive sulfide deposits: an overlooked sub-class of VMS deposit forming in complex tectonic environments. Earth-Sci. Rev. 224, 103891.

Pedersen, R.B. and Bjerkgård, T. (2016). Seafloor massive sulphides in Arctic waters. In: Rognvald, B., Bjerkgård, T., Nordahl, B. and Schiellerup, H. (Eds.) *Mineral resources in the Arctic*. Trondheim: Geological Survey of Norway, pp. 210–215.

Pedersen, R.B., Thorseth, I.H., Nygård, T.E., Lilley, M.D. and Kelley, D.S. (2010b). Hydrothermal activity at the Arctic Mid-Ocean Ridges. In: Rona, P.A., Devey, C.W., Dyment, J. and Murton, B.J. (Eds.) *Diversity of hydrothermal systems on slow spreading ocean ridges*. AGU Geophysical Monograph 188, pp. 67–89.

Pedersen, R.B., Rydland Olsen, B., Barreyre, T., Bjerga, A., Denny, A., Heggernes Eilertsen, M., Fer, I., Haflidason, H., Thomassen Hestetun, J., Jørgensen, S., Ribeiro, P.A., Steen, I.H., Stubseid, H., Tandberg, A.H.S. and Thorseth, I. (2021). Fagutredning mineralressurser i Norskehavet: landskapstrekk, naturtyper og bentiske økosystemer. Norwegian Petroleum Directorate, 128 p. Available at: https://www.npd.no/globalassets/1-npd/fakta/havbunnsmineraler/fagutredning-mineralressurser-norskehavet-naturforhold-uib.pdf [Accessed 16th May 2022].

Pedersen, R.B., Rapp, H.T., Thorseth, I.H., Lilley, M.D., Barriga, F.J.A.S., Baumberger, T., Flesland, K., Fonseca, R., Früh-Green, G.L., Jorgensen, S.L., 2010a. Discovery of a black smoker vent field and vent fauna at the Arctic Mid-Ocean Ridge. Nat. Commun. 1, 126.

Pelleter, E., Fouquet, Y., Etoubleau, J., Cheron, S., Labanieh, S., Josso, P., Bollinger, C., Langlade, J., 2017. Ni-Cu-Co-rich hydrothermal manganese mineralization in the Wallis and Futuna back-arc environment (SW Pacific). Ore Geol. Rev. 87, 126–146.

Peltonen, P., Kontinen, A., Huhma, H., Kuronen, U., 2008. Outokumpu revisited: new mineral deposit model for the mantle peridotite-associated Cu–Co–Zn–Ni–Ag–Au sulphide deposits. Ore Geol. Rev. 33, 559–617.

Petavratzi, E., Gunn, A.G., Kresse, C., 2019. Cobalt. British Geol. Survey Commod. Rev. 72 p. Available at: https://www.bgs.ac.uk/mineralsuk/search/home.html [Accessed 30th January 2021].

Peter, J.M. and Scott, S.D. (1999). Windy Craggy, northwestern British Columbia; the world's largest Besshi-type deposit. In: Barrie, C.T. and Hannington, M.D. (Eds.) *Volcanic-associated massive sulfide deposits: processes and examples in modern and ancient settings*. Reviews in Economic Geology 8. Littleton: Society of Economic Geologists, pp. 261–295.

Peter, J.M., Layton-Matthews, D., Piercey, S., Bradshaw, G., Paradis, S. and Boulton, A. (2007). Volcanic-hosted massive sulphide deposits of the Finlayson Lake District, Yukon. In: Goodfellow, W.D. (Ed.) *Mineral deposits of Canada: a synthesis of major deposit types, district metallogeny, the evolution of geological provinces and exploration methods*. Special Publication 5. St John's: Geological Association of Canada, Mineral Deposits Division, pp. 471–508.

Petersen, S., Krätschell, A., Augustin, N., Jamieson, J., Hein, J.R., Hannington, M.D., 2016. News from the seabed – geological characteristics and resource potential of deep-sea mineral resources. Mar. Policy 70, 175–187.

Pruseth, K.L., Mishra, B., Bernhardt, H.J., 1999. An experimental study on cubanite irreversibility: implications for natural chalcopyrite-cubanite intergrowths. Eur. J. Mineral. 11, 471–476.

Ramboz, C., Oudin, E., Thisse, Y., 1988. Geyser-type discharge in Atlantis II Deep, Red Sea; evidence of boiling from fluid inclusions in epigenetic anhydrite. Can. Mineral. 26, 765–786.

Rohrlach, B.D., Fu, M., Clarke, J.D.A., 1998. Geological setting, paragenesis and fluid history of the Walford Creek Zn-Pb-Cu-Ag prospect, Mt Isa Basin, Australia. Aust. J. Earth Sci. 45, 63–81.

Rottier, B., Kouzmanov, K., Wälle, M., Bendezú, R., Fontboté, L., 2016. Sulfide replacement processes revealed by textural and LA-ICP-MS trace element analyses: example from the early mineralization stages at Cerro de Pasco. Peru. Econ. Geol. 111, 1347–1367.

Saintilan, N.J., Creaser, R.A., Bookstrom, A.A., 2017. Re-Os systematics and geochemistry of cobaltite (CoAsS) in the Idaho cobalt belt, Belt-Purcell Basin, USA: evidence for middle Mesoproterozoic sediment-hosted Co-Cu sulfide mineralization with Grenvillian and Cretaceous remobilization. Ore Geol. Rev. 86, 509–525.

Saintilan, N.J., Selby, D., Creaser, R.A., Dewaele, S., 2018. Sulphide Re-Os geochronology links orogenesis, salt and Cu-Co ores in the Central African Copperbelt. Sci. Rep. 8, 14946.

Sauter, D., Cannat, M., Rouméjon, S., Andreani, M., Birot, D., Bronner, A.,Brunelli, D., Carlut, J., Delacour, A., Guyader, V., MacLeod, C.J., Manatschal, G., Mendel., V., Ménez, B., Pasini, V., Ruellan, E. and Searle, R. (2013). Continuous exhumation of mantle-derived rocks at the Southwest Indian Ridge for 11 million years. Nat. Geosci. 6, 314–320.

Schandl, E.S., 2004. The role of saline fluids base-metal and gold mineralization at the Cobalt Hill prospect northeast of the Sudbury Igneous Complex, Ontario: a fluid-inclusion and mineralogical study. Can. Mineral. 42, 1541–1562.

Schmidt, M.A., Leybourne, M.I., Peter, J.M., Petts, D., Jackson, S.E. and Layton-Matthews, D. (2021). Development of a laser ablation ICP-MS method for the analysis of fluid inclusions associated with volcanogenic massive sulfide deposits. Geochem.: Explor. Environ. Anal. 21, geochem2020-043.

Seeger, C.M. (2008). History of mining in the Southeast Missouri Lead District and description of mine processes, regulatory controls, environmental effects, and mine facilities in the Viburnum Trend subdistrict. In: Kleeschulte, M.J. (Ed.) *Hydrologic investigations concerning lead mining issues in southeastern Missouri*. U.S. Geological Survey Scientific Investigations Report 2008–5140.

Shedd, K., McCullough, E., Bleiwas, D., 2017. Global trends affecting the supply security of cobalt. Min. Eng. 69, 37–42.

Slack, J.F., 2012. Strata-bound Fe-Co-Cu-Au-Bi-Y-REE deposits of the Idaho cobalt belt: multistage hydrothermal mineralization in a magmatic-related iron oxide copper-gold system. Econ. Geol. 107, 1089–1113.

Slack, J.F., Kimball, B.E. and Shedd, K.B. (2017). Cobalt. In: Schulz, K.J., DeYoung, J.H., Seal, R.R. and Bradley, D.C. (Eds.) *Critical Mineral Resources of the United States—Economic and Environmental Geology and Prospects for Future Supply*. U.S. Geological Survey Professional Paper 1802–F.

Smith, C.G., 2001. Always the bridesmaid, never the bride: cobalt geology and resources. Appl. Earth Sci. 110, 75–80.

Snook, B., Drivenes, K., Rollinson, G.K., Aasly, K., 2018. Characterisation of mineralised material from the Loki's Castle hydrothermal vent on the Mohn's Ridge. Minerals 8, 576.

Snow, J., Hellebrand, E., Jokat, W., Mühe, R., 2001. Magmatic and hydrothermal activity in Lena Trough, Arctic Ocean. Eos 82, 193–198.

Sovacool, B.K., 2019. The precarious political economy of cobalt: balancing prosperity, poverty, and brutality in artisanal and industrial mining in the Democratic Republic of the Congo. Extr. Ind. Soc. 6, 915–939.

Stenløkk, J., Bering, D., Sandstå, N.R., Brekke, H. and Bjørnestad, A. (2019). The Norwegian Petroleum Directorate's seabed mapping of Fe-Mn crusts and massive sulphide deposits. In: *Proceedings of the 33rd Geological Winter Meeting, 7–9 January 2019, Bergen, Norway*. Trondheim: Geological Society of Norway, pp. 95.

Strmić Palinkaš, S., Pedersen, R.B. and Sahlström, F. (2020). Sulfide mineralization and fluid inclusion characteristics of active ultramafic- and basalt-hosted hydrothermal vents located along the Arctic Mid-Ocean Ridges (AMOR). In: *Proceedings of the 2020 Goldschmidt Conference, 21–26 June 2020 (virtual)*. Geochemical Society and the European Association of Geochemistry, abstract nr. 2472. https://doi.org/10.46427/gold2020.2472.

Susak, N.J., Crerar, D.A., 1985. Spectra and coordination changes of transition metals in hydrothermal solutions: implications for ore genesis. Geochim. Cosmochim. Acta 49, 555–564.

Tang, P.Z., Wang, Y.W., Wang, J.B., Long, L.L., Liao, Z., 2012. Geochemical characteristics of cobalt from the Cihai ore district, Xinjiang and their significance. Acta Mineral. Sin. 32, 379–385.

Taylor, C.D., Causey, J.D., Denning, P.D, Hammarstrom, J.M., Hayes, T.S., Horton, J.D., Kirschbaum, M.J., Parks, H.L., Wilson, A.B., Wintzer, N.E. and Zientek, M.L. (2013). *Descriptive models, grade-tonnage relations, and databases for the assessment of sediment-hosted copper deposits—with emphasis on deposits in the Central African Copperbelt, Democratic Republic of the Congo and Zambia*. U.S. Geological Survey Scientific Investigations Report 2010–5090–J.

Trilogy Metals. (2019). *Mineral resources for the Arctic & Bornite projects*. Available at: https://trilogymetals.com/assets/docs/2019-01-23-Resources.pdf [Accessed 30th January 2021].

Toffolo, L., Nimis, P., Tret'yakov, G.A., Melekestseva, I.Y., Beltenev, V.E., 2020. Seafloor massive sulfides from mid-ocean ridges: exploring the causes of their geochemical variability with multivariate analysis. Earth-Sci. Rev. 201, 102958.

Tornos, F., Heinrich, C.A., 2008. Shale basins, sulfur-deficient ore brines and the formation of exhalative base metal deposits. Chem. Geol. 247, 195–207.

Trefry, J.H., Butterfield, D.B., Metz, S., Massoth, G.J., Trocine, R.P., Feely, R.A., 1994. Trace metals in hydrothermal solutions from Cleft segment on the southern Juan de Fuca Ridge. J. Geophys. Res. Solid Earth 99, 4925–4935.

Upchurch, L., Edmonds, H.N., Resing, J., Nakamura, K., Buck, N., Liljebladh, B., Stranne, C., Tupper, G. and Winsor, P. (2007). Geochemical characterization of hydrothermal plume fluids from peridotite- and basalt-dominated regions of the ultra-slow spreading Gakkel Ridge, *Eos, Transactions, American Geophysical Union*, 88, Fall Meeting Abstracts, OS43A-0993.

U.S. Geological Survey. (2022). Cobalt. In: *Mineral Commodity Summaries 2022*. U.S. Geological Survey, pp. 53.

Vanhanen, E. (2001). Geology, mineralogy and geochemistry of the Fe-Co-Au-(U) deposits in the Paleoproterozoic Kuusamo schist Belt, northeastern Finland. PhD Thesis, Geological Survey of Finland Bulletin 399.

Vasilopoulos, M., Lefebvre, M., Molnár, F., Richard, A. and André-Mayer, A-S. (2016). Hydrothermal alteration and sources of fluids in the Juomasuo Au-Co deposit, Kuusamo Schist Belt, Finland. In: *Proceedings of the 32nd Nordic Geological Winter Meeting, 13–15 January 2016, Helsinki, Finland*. Bulletin of the Geological Society of Finland, Special Volume 1, pp. 119.

Vasyukova, O.V., Williams-Jones, A.E., 2022. Constraints on the genesis of cobalt deposits: part II. Applications to natural systems. Econ. Geol. 117, 529–544.

Vaughan, D.J., 1979. Sedimentary geochemistry and mineralogy of the sulphides of lead, zinc, copper and iron and their occurrence in sedimentary ore deposits. In: Wolf, K. H. (Ed.), Handbook of Strata-bound and Stratiform Ore Deposits. Elsevier, Amsterdam, pp. 317–363.

Vaughan, D.J., Craig, J.R., 1978. Mineral chemistry of metal sulfides. Cambridge University Press, Cambridge.

Vaughan, D.J., Rosso, K.M., 2006. Chemical bonding in sulfide minerals. Rev. Mineral. Geochem. 61, 231–264.

Von Damm, K.L., 1990. Seafloor hydrothermal activity: black smoker chemistry and chimneys. Annu. Rev. Earth Planet. Sci. 18, 173–204.

Von Damm, K.L., Edmond, J.T., Measures, C.I., Grant, B., 1985. Chemistry of submarine hydrothermal solutions at Guaymas Basin, Gulf of California. Geochim. Cosmochim. Acta 49, 2221–2237.

Von Damm, K.L., Buttermore, L.G., Oosting, S.E., Bray, A.M., Fornari, D.J., Lilley, M.D., Shanks III, W.C., 1997. Direct observation of the evolution of a seafloor 'black smoker' from vapor to brine. Earth Planet. Sci. Lett. 149, 101–111.

Von Damm, K. (1995). Controls on the chemistry and temporal variability of seafloor hydrothermal fluids. In: Humphris, S.E., Zierenberg, R.A., Mullineaux, L.S. and Thomson, R.E. (Eds.) *Seafloor hydrothermal systems: physical, chemical, biological, and geological interactions*. AGU Geophysical Monograph 91, pp. 222–247.

Wang, Y., Han, X., Petersen, S., Jin, X., Qiu, Z., Zhu, J., 2014. Mineralogy and geochemistry of hydrothermal precipitates from Kairei hydrothermal field, Central Indian Ridge. Mar. Geol. 354, 69–80.

Wang, Y., Han, X., Petersen, S., Frische, M., Qiu, Z., Cai, Y., Zhou, P., 2018. Trace metal distribution in sulfide minerals from ultramafic-hosted hydrothermal systems: examples from the Kairei Vent Field, Central Indian Ridge. Minerals 8, 526.

Webber, A.P., Roberts, S., Murton, B.J., Hodgkinson, M.R., 2015. Geology, sulfide geochemistry and supercritical venting at the Beebe Hydrothermal Vent Field. Cayman Trough. Geochem. Geophys. Geosystems 16, 2661–2678.

Williams-Jones, A.E., Vasyukova, O.V., 2022. Constraints on the genesis of cobalt deposits: part I. Theoretical considerations. Econ. Geol. 117, 513–528.

Wilson, S.A., Ridley, W.I., Koenig, A.E., 2002. Development of sulfide calibration standards for the laser ablation inductively-coupled plasma mass spectrometry technique. J. Anal. At. Spectrom. 17, 406–409.

Xu, J., Cook, N.J., Ciobanu, C.L., Li, X., Kontonikas-Charos, A., Gilbert, S., Lv, Y., 2021. Indium distribution in sphalerite from sulfide–oxide–silicate skarn assemblages: a case study of the Dulong Zn–Sn–In deposit, Southwest China. Miner. Depos. 56, 307–324.

Zaccarini, F., Garuti, G., 2008. Mineralogy and chemical composition of VMS deposits of northern Apennine ophiolites, Italy: evidence for the influence of country rock type on ore composition. Mineral. Petrol. 94, 61–83.

Zheng, J., Mao, J., Yang, F., Chai, F., Zhu, Y., 2017. Mineralogy, fluid inclusions, and isotopes of the Cihai iron deposit, eastern Tianshan, NW China: implication for hydrothermal evolution and genesis of subvolcanic rocks-hosted skarn-type deposits. Ore Geol. Rev. 86, 404–425.

Zhou, L., Zeng, Q., Liu, J., Duan, X., Sun, G., Wang, Y., Chen, P., 2020. Tracing mineralization history from the compositional textures of sulfide association: a case study of the Zhenzigou stratiform Zn-Pb deposit, NE China. Ore Geol. Rev. 126, 103792.